

1 Submitted to *Journal of Geophysical Research: Earth Surface* for possible publication

2

3 Title: A catastrophic flowslide overridden on liquefied substrate: The 1983 Saleshan

4 landslide, China

5 Authors: Fanyu Zhang<sup>a\*</sup>, Jianbing Peng, Xiugang Wu<sup>a</sup>, Fazhen Pan<sup>a</sup>, Yao Jiang<sup>c</sup>, Chao

6 Kang<sup>d</sup>, Weijiang Wu<sup>e</sup>, Wenguo Ma<sup>f</sup>

7 Affiliation:

8 (a) MOE Key Laboratory of Mechanics on Disaster and Environment in Western  
9 China; Department of Geological Engineering, Lanzhou University, Lanzhou 730000,  
10 China

11 (b) Department of Geological Engineering, Chang'an University, Xi'an 710054, China

12 (c) Key Laboratory of Mountain Hazards and Surface Process, Institute of Mountain  
13 Hazards and Environment, Chinese Academy of Sciences, Chengdu 610041, China

14 (d) Department of Civil and Environmental Engineering, University of Alberta,  
15 Edmonton, Alberta T6G 2W2, Canada

16 (e) Geological Hazards Research and Prevention Institute, Gansu Academy of  
17 Sciences, Lanzhou 730000, China

18 (f) School of Physics and Electronic-Electrical Engineering, Ningxia University,  
19 Yinchuan 750021, China

20 \*: Corresponding author

21 Email: zhangfy@lzu.edu.cn (Fanyu Zhang), dicexy\_1@chd.edu.cn (Jianbing Peng),

22 mwg@nxu.edu.cn (Wenguo Ma)

23 Title: A catastrophic flowslide overridden on liquefied substrate: The 1983 Saleshan  
24 landslide in China

25

26 Authors: Fanyu Zhang, Jianbing Peng, Xiugang Wu, Fazhen Pan, Yao Jiang, Chao Kang,  
27 Weijiang Wu, Wenguo Ma

28

29 **Abstract:** A flowslide overriding liquefied substrate can vastly enhance its disaster  
30 after failure initiation, due to rapid velocity and long-runout distance during  
31 landslides mobilized into flows. It is crucial to provide improved understanding to the  
32 mechanism of these catastrophic flowslides for hazard mitigation and risk  
33 assessment. This study focuses on the Saleshan landslide of Gansu in China, which is  
34 a typically catastrophic flowslide overrode a liquefied sand substrate.  
35 Geomorphologic and topographic maps along with analysis of seismic signals confirm  
36 its dynamic features and mobilized behaviors. ERT surveying detected abundant  
37 groundwater in the landslide, which is fundamental to its rapid long-runout distance.  
38 Particle size distributions and triaxial shear behaviors affirmed more readily liquefied  
39 behavior of superficial loess and underlying alluvial sand than red soil sandwiched  
40 them. We also examined the liquefaction susceptibility of the alluvial sand under  
41 loading impact at undrained and drained conditions. The alluvial sand is readily  
42 liquefied in the undrained condition while it is difficult at drained condition due to  
43 rapid water pore pressure dissipation. The results showed that the landslide  
44 experienced a sudden transformation from slide on the steep slope where it

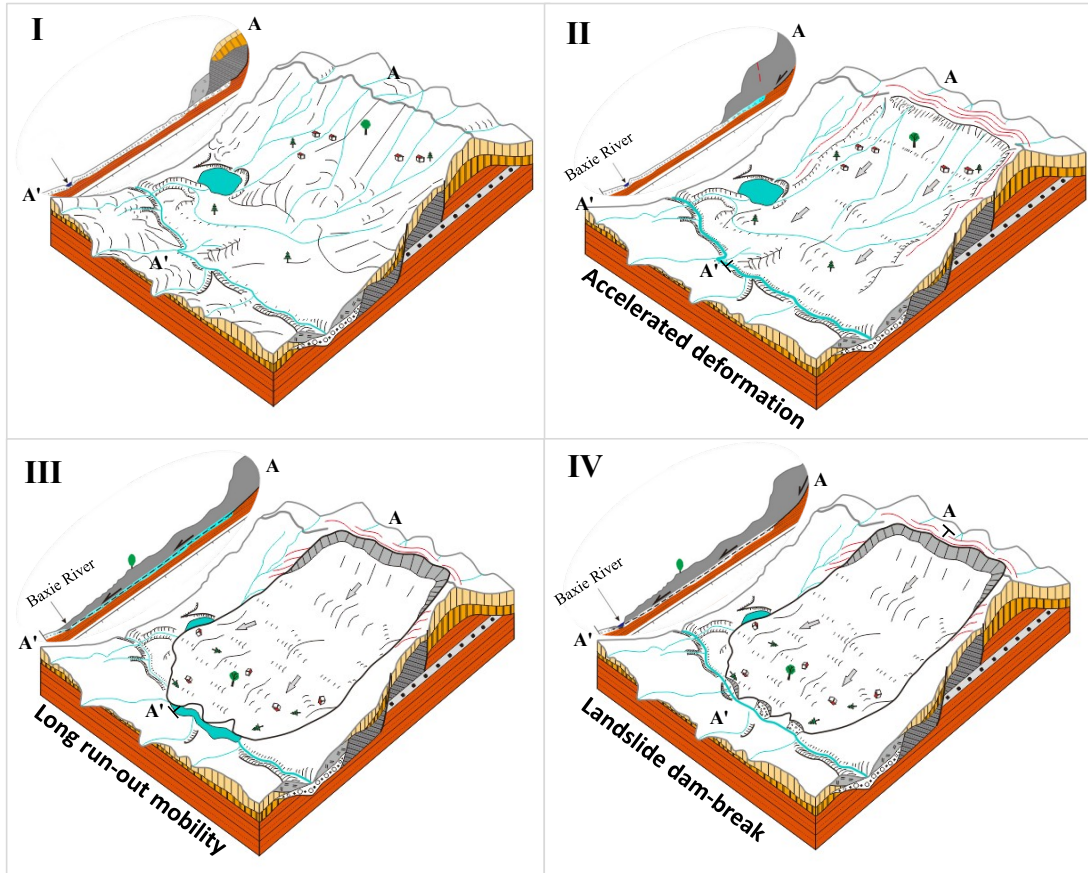
45 originated to flow on a nearly flat terrace with abundant groundwater that it  
46 overrode. This transformation can be attributed to the liquefied alluvial sand  
47 substrate enhancing the whole landslide body mobility. Along with recent, similar  
48 findings from landslides worldwide, substrate liquefaction may present a widespread,  
49 significant increase in landslide hazard and consequent mobility and our study  
50 reveals conditions necessary for this phenomenon to occur.

51

52 **Keywords:** Catastrophic flowslide, liquified substrate, mobilized transformation,

53 Saleshan landslide, China

54



56

57

58 **1. Introduction**

59 Flowslide is generally catastrophic worldwide. This kind of flow-like landslides is  
60 always characterized by rapid velocity and long-runout distance during landslides  
61 mobilized into flows, as such they usually cause more catastrophic threats to people,  
62 environment, and property. Hence, it is curial to understand the mobility of these  
63 catastrophic flowslides to hazard mitigation and risk assessment.

64 Some studies have been conducted to gain understanding of rapid long-runout  
65 flowslides, involving field evidences, numerical and physical simulations, and shear  
66 tests, along with very few field monitoring (Hutchinson and Bhandari, 1971; Misfeldt  
67 *et al.*, 1991; Evans *et al.*, 2001; Wang *et al.*, 2003; Hungr and Evans, 2004; Crosta *et*  
68 *al.*, 2009a; Poschinger and Kippel, 2009; Iverson *et al.*, 2011; Crosta *et al.*, 2015;  
69 Iverson *et al.*, 2015; Collins and Reid, 2020). However, mechanisms resulting in  
70 flowslide mobility remain in debate, but some basic information is relatively clear.  
71 These studies showed that the catastrophic flowslides commonly occur a  
72 transformation from slide to flow. Furthermore, the transformed progress generally  
73 involves an undrained loading by overlying landslide mass, which is more prevalent  
74 in granular materials, such as sand, silt, and debris, along the flow path (Hutchinson  
75 and Bhandari, 1971; Wang *et al.*, 2003; Sassa and Wang, 2005). The liquefaction of  
76 the granular materials is crucial to maintain rapid and long-runout landside mobility  
77 (Hutchinson and Bhandari, 1971; Evans *et al.*, 2001; Take and Beddoe, 2014).  
78 Furthermore, the liquefied substrates have been considered vital to the transformed  
79 landslide mobility (Iverson *et al.*, 1997; Wang *et al.*, 2003; Iverson *et al.*, 2011).

80 Nevertheless, Mangeney (2011) argued that flow-like mobility could also occur in  
81 completely dry granular materials due to the lack of cohesion. Essentially, the  
82 mobility depends finally on the frictional or rheologic behaviors of sheared granular  
83 materials. Additionally, the transformation progress occurs in a channeling flow path,  
84 but also on a nearly flat surface. The former has been the focus of considerable  
85 research effort in recent years. In comparison, only few studies examined the  
86 transformation during movement from steep upper regions onto very flat slopes,  
87 focusing on the base liquefaction of the flat flow path (Hutchinson and Bhandari,  
88 1971; Take and Beddoe, 2014; Crosta *et al.*, 2015). The 2014 Oso landslide obtained  
89 widespread attention to the catastrophic long-runout mobility on a nearly flat  
90 surface, due to the apparent presence of a liquified substrate (Iverson *et al.*, 2015;  
91 Iverson and George, 2016; Wartman *et al.*, 2016; Aaron *et al.*, 2017; Stark *et al.*,  
92 2017; Collins and Reid, 2020). However, understanding the mobility of the flowslide  
93 on a nearly flat surface remains unclear, as evidenced by the broad range of  
94 hypotheses proposed to explain the well-studied Oso landslide's mobility.

95 Loess flowslides are among the most common of the flow-like landslides, as  
96 loess is prone to liquefaction under even an unsaturated condition. Earthquake and  
97 rainfall, along with irrigation, have become familiar triggers of the catastrophic loess  
98 flowslides in China. Earthquake-induced loess flowslides generally have long-runout  
99 mobility if shallow groundwater conditions are present, resulting in liquefied loess  
100 with high pore-water pressure and low shear resistance (Ishihara *et al.*, 1990; Wang  
101 *et al.*, 2014). Currently, rainfall and irrigation become more frequent triggers to the

102 loess flowslides. Many studies showed that infiltrated water elevates the  
103 groundwater, and cause the loess liquefaction forming the loess flowslides  
104 (Derbyshire *et al.*, 2000; Zhang *et al.*, 2014; Zhuang and Peng, 2014; Peng *et al.*,  
105 2015; Peng *et al.*, 2017a; Peng *et al.*, 2017b; Zhang *et al.*, 2017; Zhang and Wang,  
106 2018; Peng *et al.*, 2019). Visibly, water plays a dominant role in the occurrence of the  
107 loess flowslides. These studies mentioned above significantly improved our  
108 understanding of loess flowslides. Still, much of this effort has been in their initiation  
109 and failure mechanisms, examining the liquefied behavior of the loess. Some studies  
110 of the mobility of the loess flowslides focused on numerical simulation and field  
111 evidence (Peng *et al.*, 2015; Zhang *et al.*, 2017; Kang *et al.*, 2018; Li *et al.*, 2019). Yet  
112 there still remains an urgent problem to understand the mobilized mechanisms of a  
113 landslide from a slide on the steep upper slope that transforms into a flow on a  
114 nearly flat terrace. Such slides frequently threatened the residents and their  
115 properties, and also cause major ecological and environmental problems.

116       This study aims to provide an improved understanding of the transformed  
117 mechanism from slide to flow overridden on a liquified substrate. We study a  
118 catastrophic flowslide, i.e., the Saleshan landslide of Gansu in China, which killed .  
119 We produced geomorphologic and topographic maps for analyzing the movement  
120 features of the landslide using cartographic and GIS techniques. We performed  
121 electrical resistivity tomography (ERT) to detect groundwater conditions on the  
122 landslide body and the terrace. Furthermore, we examined the particle size  
123 distributions and triaxial shear behaviors of loess, red soil, and alluvial sand from the

124 landslide deposited zones. We especially performed two loading impact tests on the  
125 alluvial sand specimens under drained and undrained status. Finally, we discussed  
126 the transformed mechanism of this kind of landslide from slide on steep slopes to  
127 flow on gentle terraces, and compare the difference in the liquified entrainment  
128 occurred in a steep channel bed erosion along its flow path. Our findings afford some  
129 fundamental knowledge to the mobility of this kind of flowslides overridden on a  
130 liquefied substrate, and specific assistances for landslide hazard mitigation and risk  
131 assessment.

132

## 133 **2. Saleshan landslide background**

134 The Saleshan landslide is situated in Dongxiang County, Gansu Province, China  
135 (Fig. 1a), and occurred on an afternoon at about 5:46 local time on 7 March 1983,  
136 which caused 237 deaths and damage of the four villages. Hence, the Saleshan  
137 landslide is among the most disastrous one in the Baxie River catchment, which has  
138 hundreds of different types of loess landslides at various sizes (Fig. 1b). Following the  
139 updated Varnes landslide classification system, Hungr *et al.* (2014) described the  
140 Saleshan landslide as a flowslide, which is characterized by long runout distance  
141 traveled across a nearly flat surface. Fig. 1 c and d present the panoramic views of  
142 the Saleshan landslide in 1983 and 2015.

143

### 144 **2.1 Geological structures**

145 Fig. 2 shows the simplified stratigraphic and topographic section through the  
146 pre-landslide topography and the Saleshan landslide along its main sliding direction.  
147 The presented stratigraphic and topographic section is revised to the previous  
148 version from Zhang and Wang (1984) and Zhang *et al.* (2002). The geological  
149 structures can be referred to in the previous studies (Zhang and Wang, 1984; Zhang  
150 *et al.*, 2002).

151 To geological structures before failure (Fig. 2a), the stratigraphic section of the  
152 Saleshan landslide include in descending order: (1) Late Pleistocene Lishi Loess ( $Q_2$ ),  
153 (2) Middle Pleistocene Malan Loess ( $Q_3$ ), (3) Pliocene mudstone and Cobblestone  
154 ( $N_2$ ), (4) Quaternary alluvial sand and gravel, colluvial mudstone and loess ( $Q_4$ ). The  
155 alluvial sand and gravel is located on the first terrace. Moreover, the previous studies  
156 speculated that the colluvial mudstone and loess is the deposition of a historical  
157 landslide situated over the first terrace (Kang *et al.*, 2018). There are no folds and  
158 faults in Saleshan landslide area, which exhibits a simple geologic structure (Zhang *et al.*,  
159 2002). Nevertheless, there are two sets of dominant joints, in which the east-  
160 west set is matched with cracks in the main scarp of Saleshan landslide (Zhang *et al.*,  
161 2002).

162 To geological structures after failure (Fig. 2b), a simplified stratigraphic section  
163 can be described as follow: (1) the displaced material of landslide body covered over  
164 the alluvial sand and gravel on the first terrace; and (2) the alluvial layer overlies the  
165 undisturbed mudstone bedrock. Zhang *et al.* (2002) considered that the alluvial sand  
166 and gravel is undisturbed on the first terrace, while other authors argued that the

167 landslide ploughed or impacted the alluvial layer, leading to erosional liquefaction of  
168 the substrate (Wang *et al.*, 1988; Kang *et al.*, 2018). It is interesting to note the life-  
169 saving tree on the landslide. When the Saleshan landslide occurred, a person tightly  
170 held the tree, moving about 960 m without any injuries (Zhang *et al.*, 2002; Kang *et*  
171 *al.*, 2018).

172

### 173 **2.1 Geomorphologic characteristics**

174 The Saleshan landslide is located on the south facing side of a steep slope ridge  
175 on the northern side of Baxie River. The geomorphologic characteristic change of the  
176 Saleshan landslide mainly depends on the Baxie River terraces (Fig. 2). The elevation  
177 of the Saleshan landslide ranges from 1950 m to 2280 m, including four terraces with  
178 abrupt slope angle change. The top of the slope ridge is 2280 m elevation above the  
179 fourth terrace, where the slope angle is larger than 50°. The fourth terrace is located  
180 between 2195 m and 2080 m elevation, with a slope angle varying from 30° to 35°.  
181 The third and second terraces have developed two gentle platforms, and their  
182 elevation varies from 2080 m to 1970 m with a switched deep slope with an average  
183 30° slope angle. The lowest first terrace is about 800 m away from the toe of the  
184 Saleshan slope with nearly flat surface topography before slope failure. After the  
185 Saleshan slope failure, the first terrace became the main accumulation zone. The  
186 topographic change reveals that the Saleshan landslide failed from a deep upslope  
187 and moved on a flat surface with easy liquified sand and gravel layer, which means an  
188 abrupt transformation of movement style. This also indicates that the geologic

189 structure and geomorphologic characteristics is basic conditions for the long-runout  
190 mobility during Saleshan landslide propagation.

191

### 192 **2.3 Hydroclimatic conditions**

193 The Baxie River basin is a semiarid climate environment. Commonly, the average  
194 annual precipitation is 485 mm, with 80% of the total in the period from June to  
195 September, and frequent rainstorms in summer (Zhang *et al.*, 2002; Kang *et al.*,  
196 2018). However, the climate presents a wetter environment since 1979, with annual  
197 precipitation of 650 mm, and the winter precipitation in 1982 was also above  
198 average reaching 66.3 mm (Zhang *et al.*, 2002). There has meltwater before failure in  
199 March 1983. Thus, the freeze-thaw effect was suggested to trigger the Saleshan  
200 landslide (Huang, 2009). However, Kang *et al.* (2018) considered that the meltwater  
201 effectively elevated groundwater, which would be attributed to progressive failure.

202 The groundwater is of phreatic water, which has all distributed below the fourth  
203 terrace (Ma and Qian, 1998). Many springs overflow from the toe of the terraces on  
204 both sides of the River valley. Notably, the shallow aquifer on the first terrace is  
205 known from borehole information, and the depth of the groundwater table is about  
206 2 m below the ground surface (Ma and Qian, 1998). Besides, the storage water in the  
207 Jiuer reservoir was used to the agricultural irrigation on the terraces, guaranteeing  
208 the long-term shallow groundwater level. The groundwater information provides  
209 useful help to understand the mobility of the Saleshan landslide.

210 Notably, no observed earthquake and rainfall was recorded in the Baxie River

211 basin in March 1983. Therefore long-term accumulated precipitation and irrigation,  
212 rather than abrupt seismic shaking and rainfall infiltration, likely played a key role in  
213 initiating the Saleshan landslide.

214

### 215 **3. Materials and methods**

#### 216 **3.1 Geomorphological features mapping**

217 The geomorphological mapping provides geomorphologic characteristics as an  
218 important aid for understanding the inherent problems on the propagation of the  
219 landslide. For this purpose, we collected various data from old photos, field  
220 investigations, remote images, previous references about Selanshan landslide, and  
221 produced a graphical map of geomorphologic imprints using cartographic and GIS  
222 techniques. The geomorphological map in this study is representative of many results  
223 both from various published data and unpublished reports.

224

#### 225 **3.2 Topographic changes detection**

226 The topographic change detection is a fundamental prerequisite for landslide  
227 deposition thickness but also can provide a direct result assessment for landslide  
228 numerical modeling. In this context, we first prepared two large scale topographic  
229 maps at the scale of 1:10000 from before and after slope failure, and digitized the  
230 two maps using ArcGIS software, and then constructed their digital elevation models  
231 (DEMs). After which, we compared and analyzed the topographic change using the  
232 Geomorphic Change Detection (GCD) 7.0 software (<http://gcd.riverscapes.xyz/>),

233 which is a powerful tool on geomorphological change detection (Wheaton *et al.*,  
234 2010; Wheaton *et al.*, 2015). The GCD produced DEM of Difference (DoD) maps  
235 before and after the Saleshan landslide, and estimated the net change in  
236 geomorphologic features, such as elevation, volume, area.

237

### 238 **3.3 Movement features analysis**

239 To analyze mobility after slope failure, we produce a map of movement features,  
240 including motion displacement, motion direction, and motion velocity. The motion  
241 displacement derives a direct estimate from the placemarks on landslide body,  
242 including the sites from house and tree before and after failure. We also record the  
243 motion direction of all the placemarks referred to the previous research results  
244 (Wang *et al.*, 1988). We also calculated the motion velocity from displacement over  
245 time at different sites of the Saleshan landslide. The mobility time derives from  
246 seismic signals induced by Saleshan landslide at three seismic stations. The detailed  
247 procedure can refer to the supplementary, involving how to digitize old analog  
248 seismograms to obtain the relatively accurate time using a MATLAB™ toolbox of  
249 DigitSeis developed by Bogiatzis (2015), with slight help of manual processing, to  
250 revitalize only three NS analog seismograms from the three seismic stations  
251 (Supplementary note, Figs. 1 and 2).

252

### 253 **3.4 Textural and mechanical properties test**

254 To obtain the textural and mechanical properties, we taken disturbed loess and

255 red soil (product of mudstone) specimens close to the scarp of the Saleshan  
256 landslide, as well as an alluvial sand specimen on the first terrace of Baxie River.  
257 These specimens were oven-dried and disaggregated using a rubber hammer. We  
258 analyzed particle size distributions of all the samples using a Microtrac S3500 laser  
259 diffraction instrument. Each specimen tested eight times for consistency.

260 We conducted a series of consolidated undrained compression (CUC) triaxial  
261 tests on all the three samples, and two quasi-dynamic impact stress loading (QSL)  
262 drained and undrained triaxial tests on the alluvial sand samples. All the specimens  
263 have a height of 10 cm and a diameter of 5 cm. All the examples were saturated by  
264 carbon dioxide replacement, de-aired water flushing, and back pressure saturation.  
265 The specimens were consolidated under a specified cell pressure and then  
266 compressed under undrained conditions by means of the strain-controlled method.  
267 The axial strain was increased at a rate of 0.01% per minute. The specimens were  
268 consolidated and tested at cell pressures of 100, 200, 300 kPa. In CUC sets,  
269 compression at each cell pressure was terminated when the axial strain close to 20%.  
270 In QSL sets, the specimens were compressed by utilizing a sinusoidal stress loading  
271 module, but in which we used a quarter loading period to load 160 kPa with 10  
272 seconds at cell pressures of 200 kPa. Notably, if the stress loading velocity is too  
273 rapid, this maybe generates a damage to the triaxial apparatus. We performed one  
274 drained stress loading test, and other for the undrained condition.

275

### 276 **3.5 Electrical resistivity survey**

277 To prospect the internal structure and hydrological environment of the Saleshan  
278 landslide, we carried out four electrical resistivity tomography (ERT) profiles (see  
279 their locations in Fig. 5) to obtain a detailed characterization about the electrical  
280 signals in the first tens of meters below the ground surface. During the field survey,  
281 we used a multielectrode system with 120 electrodes both in Wenner-Schlumberger  
282 and Wenner arrays with an electrode spacing of 5 m. We located these electrical  
283 profiles using a GPS and measured their topographic changes using a laser measuring  
284 technique. Finally, we inverted the apparent resistivity data by a tomographic  
285 inversion technique using the newest RES2DINV software. During the inversion, we  
286 implemented a smoothness-type regularization constrained least squares by using  
287 incomplete Gauss-Newton optimization technique, taking the topographical changes  
288 into account along the profiles. The optimization technique is to iteratively adjust the  
289 resistivity to obtain a minimal difference between the calculated and measured  
290 apparent resistivity values. The absolute acceptable error provides a measurement of  
291 this difference.

292

## 293 **4. Results**

### 294 **4.1 Geomorphologic imprints**

295 The geomorphologic imprints on a landslide provide direct observation and  
296 object analysis for dynamic features at different zones, but is important base to  
297 hazard management land planning after the landslide. Fig. 3 shows the  
298 geomorphological map of Saleshan landslide, which is a revised version based on the

299 previous conclusions (Zhang *et al.*, 2002; Wu and Wang, 2006). Our  
300 geomorphological map presents an immediate and complete description of  
301 remaining features at different locations throughout the landslide. From the  
302 viewpoint of space elements, we divide the geomorphologic features into three  
303 styles. The dotted imprints only have spring outcrop places. The linear features  
304 include zone boundaries, major and minor scarps, various cracks, groundwater  
305 drainage, and surface water recharge. The planar features involve depressions and  
306 hillocks in the zone of depletion, and grooves and hummocks in the zone of  
307 accumulation, along with river gully and reservoir adjacent landslide.

308       There are several critical features worth analyzing. First, the different types of  
309 cracks portray the deformation behaviors at respective locations. The cracks  
310 distributed on the crown portray tensile deformation, and the lateral and transverse  
311 cracks that occurred on the flank signify tractive deformation and fracturing process.  
312 These radial cracks emerge thrust behavior on the toe. The depressions and hillocks  
313 underwent extension and compression during the landslide movement. The  
314 significant number of hummocks on the zone of accumulation show the evidence of  
315 fluidization and extension during landslide mobility. There are more in the west-slide  
316 and central regions than in the east slide in the zone of accumulation. Using  
317 hummocks that explain the motion behavior of the fluidized landslides has also been  
318 paid special attention by other authors (Paguican *et al.*, 2014; Collins and Reid, 2020;  
319 Dufresne and Geertsema, 2020). The hummocks on a landslide can reveal important  
320 movement features during their motion.

321 Fig. 4 shows the old photographs illustrating typical geomorphological imprints  
322 of the Saleshan landslide. These photographs were taken shortly after the landslide  
323 in 1983. They not only well verify the evidence from the geomorphological map (Fig.  
324 3), but some of them provide more intuitive clues to uncover movement behavior. As  
325 shown in Figs. 4c and 4d, the standing cow and life-saving tree reveal that the  
326 displaced materials were incompletely disturbed, mainly maintaining the original  
327 stratigraphic structure. Thus, we can speculate that the landslide body moved along a  
328 slip surface with low shear resistance. Also, we observe differential movement on the  
329 zone of accumulation, due to differences in disturbance and liquefaction of the  
330 displaced materials (Fig. 4i-Fig. 4l). The loess at right flank is completely liquified (Fig.  
331 4i), and the deposit at the toe dammed the Baxie River gully with high water content  
332 (Fig. 4j). While the deposit close to left flank buried the Jiuer reservoir (Fig. 4k), but  
333 they hold some original structures presenting a low water content context.

334 From the geomorphologic imprints and evidence, we suggest that the Saleshan  
335 landslide exists a motion transformation from slide to flow and that the flow-like  
336 materials failed along a weak slip surface with some differences in deposit features.  
337 Meanwhile, this evidence affords clues to analyze the characteristics of accumulation  
338 and mobility after slope failure.

339

## 340 **4.2 Topographic changes**

341 There are few accurate measurements of the volume of a historical landslide,  
342 because of a difficulty gaining the pre- and post-landslide topographic data. Fig. 5a

343 shows the elevation difference of the pre- and post-landslide on the Saleshan  
344 landslide. Fig 5b and 5c show geomorphic change detection, the areal and volumetric  
345 elevation change distributions. The negative elevation is for erosion, and positive  
346 elevation is for accumulation, respectively. The elevation change range of erosion  
347 area is -142 to 0 m, which located on the depletion zone. The elevation change range  
348 of accumulation distributes between 0 and 39 m occurred in the accumulation zone.  
349 Volume proportions of erosion and accumulation are almost the same, which are  
350 55.69 and 44.31%, respectively. The decrease of accumulation volume may be due to  
351 the part of loess flowing into Baxie river and Jieer reservoir. The areal proportion of  
352 erosion (35.11%) is about half as much as deposition (64.89%).

353 To better detect the dynamic process of landslides, such as the change of area,  
354 volume, and elevation in pre- and post-landslide, we used the Geomorphic Change  
355 Detection (GCD) 7.0 software to construct seven two-dimensional profiles of the slip  
356 surface in the movement direction and four profiles perpendicular to the movement  
357 direction (Fig. 5a). By analyzing the profiles (Fig. 6), we can further understand the  
358 characteristics of the topographic change of the Saleshan landslide. With steeper  
359 slopes, the erosion probability is higher, and the maximum erosion height up to 139  
360 meters, while the majority of accumulation occurs on the flat areas (P1-P7). It also  
361 can be found that erosion mainly occurs on the fourth terrace, and the first terrace is  
362 the accumulation zone. The accumulation and erosion features are related to the  
363 evidence from geomorphologic characteristics. For the four profiles perpendicular to  
364 the movement direction, the degree of erosion at area of P8 and P9 is much greater

365 than that of P10 and P11. As P8 and P9 is located at the trailing edge of the landslide,  
366 others are at the leading edge of the landslide. Likewise, hillocks and scarps at the  
367 trailing edge of the landslides are eroded, while gullies are piled up and filled. These  
368 profiles describe the exterior morphological features and structures in the horizontal  
369 and vertical directions, and it can highlight some changes in pre- and post-landslide.

370

### 371 **4.3 Rapid and long-runout mobility**

372 In the mobility of the rapid and long-runout landslides, its velocity,  
373 displacement, and direction are vital kinematic parameters. Nevertheless, they are  
374 often uncertain because this is practically difficult to identify the kinematic  
375 parameters accurately. However, the surviving placemarks, e.g., tree and house,  
376 could be useful in the dynamic analysis. Fig. 7 shows the motion displacement vector  
377 at different placemark locations on the Saleshan landslide, and the calculated  
378 kinematic parameters are listed in Table 1. Among these placemarks, there is the  
379 most significant motion displacement of 1090 m and the highest motions velocity of  
380 19.8 m/s. The results reveal that the Saleshan landslide underwent rapid and long-  
381 runout mobility, in which appeared apparent variable zonation of motion.

382 On the depletion zone, the three placemarks are almost the same with the  
383 horizontal displacements from 310 to 340 m, which means that the vertical fall is  
384 significant in the zone (see Fig. 1b). There has the lowest average velocity of 5.9 m/s  
385 in the whole landslide zones with a velocity between 5.8 and 6.2 m/s. Due to the  
386 calculated velocities on the total mobilized time of 55 seconds, the velocity of the

387 depletion zone may severely be underestimated in the three placemarks. The  
388 previous dynamic studies and eyewitness account showed that the velocity of the  
389 sliding blocks both exceeds 20 m/s in the depletion zone (Miao *et al.*, 2001; Zhang *et*  
390 *al.*, 2002; Kang *et al.*, 2018).

391 On the accumulation zone, the displacement vectors present distinct kinematic  
392 differences. The placemarks of the central accumulation zone have the greatest  
393 motion displacement with the highest landslide velocities. There have relatively more  
394 significant displacement and velocity on the west accumulation zone than on the  
395 east accumulation zone. It should be noted that there have relatively low velocity  
396 and small motion displacement closer to both the flanks. It is consistent with the  
397 field evidence (Fig. 4k). This means that the displaced materials immediately stop  
398 after rupturing the slide surface. In addition, the motion directions of the various  
399 placemarks depend on the original topographic changes and geomorphologic  
400 features (Fig. 3 and Fig. 4).

401 In sum, the Saleshan landslide was rapid in the progress of long-distance  
402 motion. The motion of Saleshan landslide primarily occurred on the accumulation  
403 zone, in which the velocity and displacement of the displaced materials decrease  
404 from the central zone to two flanks. The motion features are matched with the  
405 evidence from geomorphologic maps and topographic changes (Fig. 3~Fig. 6).  
406 Besides, the underestimated velocity derived from displacement and time may result  
407 in some misleading to kinematic analysis.

408

#### 409 4.4 Structural and hydrological constraints

410 ERT is widely used in landslide investigation characterized by a complex  
411 geological setting (Perrone *et al.*, 2014). And recently time-lapse ERT is increasingly  
412 applied in long-term landslide monitoring (Grandjean *et al.*, 2011; Chambers *et al.*,  
413 2013; Wilkinson *et al.*, 2016; Crawford *et al.*, 2019). Thus, ERT used as a conventional  
414 geophysical prospecting method to the geological structure and hydrological  
415 environment of a landslide, now becomes a convenient technology using in-situ  
416 landslide monitoring.

417 Fig. 8 shows the interpreted Wenner ERT sections of four profiles on the  
418 Saleshan landslide, and the detailed location of the four profiles are shown in the  
419 index figure and Fig. 6. The profile L1 is longitudinal through the front zone of  
420 depletion, and the end zone of accumulation along movement direction (Fig. 8a), and  
421 the profile C1 is transverse through the toe region of rupture surface (Fig. 8b). In  
422 addition, the interpreted Wenner Schlumberger ERT sections of four profiles are  
423 shown in Supplementary Figs 3. The profiles L1 and C2 profiles orthogonally cross  
424 through the middle zone of accumulation on the first terrace (Fig. 8c and d). In the  
425 profile L1, the high resistivity sections correspond with the front zone of depletion  
426 with relatively low water content and complete structure, while the end zone of  
427 accumulation presents low resistivity. The information disclosed from ERT image is  
428 matched with the data of borehole after the landslide (Wu and Wang, 2006), along  
429 with in-situ investigation. Notably, there is an abundant phreatic region around the  
430 rupture surface. It can be verified the evidence from the spring exposed on the third

431 and fourth terrace, along with the surface water convergence in the gully (See Fig. 3).  
432 The low resistivity in the profile C1 is consistent with the gully sites, where there has  
433 high water content in lowland causing thicker deposit and greater mobility (See Fig.  
434 6). Meanwhile, the toe zone of the rupture surface has relatively lower resistivity,  
435 comparing with the zone of depletion. The information from profiles L1 and C2  
436 shows that the displaced materials thickness vary between 15 and 20 m, and that  
437 they deposited on the original ground surface (Fig. 6). The deposit is thinner closer to  
438 the tip of the Saleshan landslide. Notably, the sediments below the farmland ground  
439 exert a very low resistivity signifying a high water content condition. This is well-  
440 matched with direct field observations after the landslide, such as loess liquefaction  
441 and deposit with high water content (see Fig 4j and Fig 4l) on the west zone of  
442 accumulation.

443 The electrical resistivity could obtain useful geophysical signals varying with the  
444 nature and state of granular materials, as well as the fluid in the granular medium.  
445 Thus, the four ERT survey images add information on the internal structure of the  
446 Saleshan landslide, which is consistent with the geomorphologic features and  
447 topographic changes. Meanwhile, the ERT images well provide the hydrological  
448 information, which helps the understanding of the propagation of the Saleshan  
449 landslide.

450

## 451 **4.5 Liquefaction behaviors**

### 452 **4.5.1 Particle size distribution**

453 The particle size distributions are often crucial for appraising liquefaction  
454 potential of flow slides (Kramer, 1988; Picarelli, 2010), and could be indirectly used to  
455 interpret liquefaction behaviors of fine granular soils. Fig. 9 shows the exemplified  
456 particle size distribution of the three types of soil on the Saleshan landslides. To  
457 facilitate a much clearer view of particle size, Fig. 9b uses a linear abscissa, rather  
458 than a logarithmic abscissa. Other repeated test results were shown in  
459 Supplementary Figs. 4. The three samples are silty soils with uniform gradation. The  
460 loess has the greatest fine fractions, and the alluvial sands include the coarsest  
461 fractions, whereas the red soil is intermediate. Note that there are two modes on the  
462 frequency curves with two unimodal curves and one bimodal curve. The loess and  
463 red soil have both a smooth unimodal frequency distribution curve. The loess has a  
464 single fine component with a size boundary of 20-60  $\mu\text{m}$  and mean practice size ( $D_{50}$ )  
465 of 38  $\mu\text{m}$ . The texture of the red soil is like that of the loess, but it has a deviation  
466 with a size range of 25-55  $\mu\text{m}$ , and a mean practice size of 43  $\mu\text{m}$ . This kind of  
467 deviation may derive from the modification of weathering processes of mudstone.  
468 The alluvial sand has a bimodal frequency distribution of particle size, and the range  
469 is from 25  $\mu\text{m}$  to 60  $\mu\text{m}$  with a mean practice size of 48  $\mu\text{m}$ . Generally, the bimodal  
470 sand is a typical production of a modern alluvial or fluvial environment (Taira and  
471 Scholle, 1979; Sun *et al.*, 2002). Compared to evidence from the particle size  
472 distribution in other flowslides (Kramer, 1988; Picarelli, 2010; Zhang *et al.*, 2019), all  
473 the three samples on the Saleshan landslide are characteristic of liquefaction  
474 features, which have the potential to liquefy when close to saturation.

475

#### 476 **4.5.2 Shear properties**

477 It is still necessary to examine the shear properties of soil to understand its  
478 liquefaction behaviors directly. Fig. 10 compares the results of the undrained triaxial  
479 shear tests of the three soils on the Saleshan landslide at the same confining  
480 pressure (i.e., 200 kPa). Fig. 10a and b present the change deviator stress and pore  
481 water pressure with axial strain. Fig. 10c depicts an effective stress path. The three  
482 specimens have apparent differences in liquefaction behaviors. The loess specimen  
483 shows a typical strain behavior maintaining high pore water pressure with an obvious  
484 decrease in strength after peak value. The results are consistent with those observed  
485 in the liquified or collapsed loess elsewhere (Zhang *et al.*, 2013; Wang *et al.*, 2014;  
486 Zhang *et al.*, 2014; Zhang and Wang, 2018). This means that the loess in Saleshan  
487 landslide area has visible liquefaction behavior under undrained condition, which is  
488 matched with in-situ evidence (Fig. 4i). Notably, the red soil has the lowest  
489 liquefaction potential with very light strength decrease after peak strength, although  
490 its particle size distribution is located between loess and alluvial sand. It may be  
491 related to the strong cementation or bonding existing in the weathering products of  
492 mudstone, which could attribute to more clay fractions in the red soil. The alluvial  
493 sand specimen has the most significant increase in pore water pressure after the  
494 peak strength. As shown in Fig. 9, the alluvial sand is comprised of fine sand, and  
495 finer suspended muddy. The small amount of suspended muddy slightly decreases  
496 the liquefaction of the alluvial sand. Similar results have been found in ring shear

497 and triaxial shear tests (Wang *et al.*, 2007; Carraro *et al.*, 2009).

498 Fig. 11 shows the undrained triaxial test results for the alluvial sand specimens.  
499 The deviator stress of all the specimens increases a peak value with increasing axial  
500 strain; after that, abruptly decreases a steady-state with further increase in axial  
501 strain (Fig. 11a). Meanwhile, the pore water pressure continuously increases to a  
502 steady value with increasing axial strain (Fig. 11b). The effective stress paths show  
503 that pure contractive behavior during undrained compression shearing (Fig. 11c).  
504 These results further support that all the alluvial sand specimens present unusual  
505 liquefaction behavior, and that is more prominent at low confining pressure.

506 Fig. 12 shows the triaxial test results from quasi-dynamic impact stress loading  
507 of the alluvial sand specimens under drained and undrained conditions. In the  
508 drained condition, the pore water pressure increases rapidly to 20 kPa in the  
509 progress of the impact loading (i.e., 10s), and after that, it has an obvious decrease  
510 with almost constant loading deviatoric stress of 160 kPa (Fig. 12a). Meanwhile, the  
511 generated pore water pressure dissipated gradually with 100 s. The relatively high  
512 dissipation rate in pore water pressure could be attributed to its inherent granular  
513 characteristics (Fig.9). This is in contrast to the behavior exhibited in undrained  
514 impact loading, and the pore water pressure is the same rapid increase as the  
515 drained impact stress loading (Fig. 12b). The desired impact stress could not fully  
516 load on the samples, and it has completely collapsed with a rapid increase in pore  
517 water pressure. After that, the pore water pressure slightly increases and,  
518 accordingly, a striking decrease in deviatoric stress. It is essential for a structural

519 collapse with a great axial displacement. The results show that impact can generate  
520 pore water pressure on the alluvial sand, and the undrained impact loading is easier  
521 to produce pore water pressure on the alluvial sand than under drained conditions.  
522 Meanwhile, the quickly dissipated pore water pressure on the alluvial sand may  
523 contribute to the liquefaction of the loess, and consequently enhanced the mobility  
524 of the Saleshan landslide. This finding is consistent with those research results from  
525 ring shear tests (Wang *et al.*, 2003) and numerical simulation (Collins and Reid,  
526 2020).

527

## 528 **4. Discussion**

### 529 **4.1 Transformation from a slide on the steep slope to flow on the gentle terrace**

530 The Saleshan landslide experienced a typical transformation from progressive  
531 slide to catastrophic flow, i.e., velocity transition from slow to fast. The progressive  
532 deformation along a sliding surface went through more than four years from the  
533 evidence of monitoring data and eyewitness account, while the disastrous mobility  
534 after failure initiation only underwent 60 seconds with about 1000 m mobility (Wang  
535 *et al.*, 1988; Miao *et al.*, 2001; Zhang *et al.*, 2002; Wu and Wang, 2006; Kang *et al.*,  
536 2018). Fig. 13 shows the hypothesized sequence from progressive deformation to the  
537 catastrophic mobility of 1983 Saleshan landslide. The stage from slow to accelerated  
538 deformation resulted in the pore water pressure accumulation in the toe zone of the  
539 slope (Fig. 13a and b). After that, the landslides on dissected steep mudstone slope  
540 transformed into a flow-type landslide that travels long runout distance across a

541 nearly flat terrace (Fig. 13c). Finally, the elevated reservoir water triggered landslide  
542 dam-break (Fig. 13d). The previous studies have well analyzed the deformation  
543 mechanism of the Saleshan landslide, but the unexpected flow-type mobility remains  
544 unclear. Thus, we focus here on the transformation mechanisms from the slide on  
545 steep upper slope to flow on nearly flat terrace.

546         The transformed landslide from slide to flow could be attributed to the unusual  
547 structural and hydrological configurations of the toe and travel zone of the Saleshan  
548 landslide. There is enough surface and sub-surface water convergence, leading to a  
549 shallow groundwater level in alluvial sand layers with high liquefaction potential on  
550 the first terrace. The evidence can prove the speculation from geomorphologic  
551 mapping (Figs 2 and 3), ERT survey (Fig 8), and test results (Figs. 9-11). Generally, the  
552 groundwater condition is key to the transformation from progressive slide to  
553 catastrophic flow in the Saleshan landslide; meanwhile, the highly susceptible to  
554 liquefaction alluvial sand is essential to the transformation. On the whole, the  
555 transformation strictly depends on the liquefied substrate, i.e., alluvial saturated or  
556 even partly saturated sand layer on the first terrace. Of course, as revealed by results  
557 in field and laboratory (Figs. 3-5 and Fig. 10), the highly liquefied loess has a  
558 particular contribution to the mobility after failure.

559         In the Chinese Loess Plateau, identical loess flowslides have frequently occurred  
560 on the Jingyang platform (Xu *et al.*, 2009; Peng *et al.*, 2017a; Peng *et al.*, 2018; Li *et*  
561 *al.*, 2019). These researchers also proved that the hydrogeological conditions on the  
562 nearly flat river terrace close to the current Wei River, i.e., the alluvial sand layer and

563 high groundwater level, control the transformed progress. Incorporating with  
564 evidences from liquefied sand pipes observed in loess deposits (Xu *et al.*, 2009)  
565 deduced a conceptualized liquefaction model in double layers (i.e., sand and loess)  
566 along sliding surface on the nearly flat terrace. Peng *et al.* (2018) excavated several  
567 big exploratory trenches on the accumulation of the flowslides, and they found  
568 typical liquefied evidence of sand pipes and sand boils intruded into loess deposits.  
569 However, it lacks direct ground evidence, which can be attributed to the thick loess  
570 deposits with relatively low permeability. Also, the numerical simulation and shear  
571 wave detection supported that liquefaction entrainment of the terrace sand deposits  
572 controls their rapid and long runout mobility of those loess flowslides (Peng *et al.*,  
573 2017a; Li *et al.*, 2019).

574 In the rest of the world, there have been similar structural and hydrologic  
575 constraints with the above loess flowslides, which resulted in the same  
576 transformation from slides on steep upper slope to flows with high mobility on a  
577 gentle lower terrace. A famous example in Switzerland is the Flims rockslide  
578 avalanche, which liquefied alluvial deposits on the terrace, leading to about 13 km  
579 displacement and damming of the Vorderrhein river valley (Poschinger and Kippel,  
580 2009). There was observed the sub-vertical tubes of gravel composition almost  
581 without any fines in the landslide deposits (Pavoni, 1968), and these finer materials  
582 such as sand and silt have been washed out during water flow (Pavoni, 1968;  
583 Poschinger and Kippel, 2009). This is a typical feature of liquefaction of alluvial  
584 deposits. The scholars in Czech Republic found that a massive rockslide avalanche

585 transformed as a long-runout landslide along the terrace in the Bilina river (Burda *et*  
586 *al.*, 2018). The data shows that the slope of the terrace is generally lower than 10  
587 degrees in this study region (Poschinger and Kippel, 2009; Burda *et al.*, 2018). In  
588 Saskatchewan river, there have many landslides dissected on shale slopes; some of  
589 them transformed into a fluidized landslide that mobilized far beyond that expected  
590 on a nearly flat terrace. Moreover, multiples boreholes revealed that the sliding  
591 surface is located on Tertiary sand in the Hepburn aquifer system (Misfeldt *et al.*,  
592 1991). Thus, enough groundwater and sand prone to liquefaction are essential to  
593 these landslides that occurred in the Saskatchewan river region. Crosta *et al.* (2015)  
594 presented multiple examples of landslides from steep slopes falling onto a shallow  
595 erodible substrate or water layer, and then travel long-runout distance with typical  
596 high velocity. Crosta and his colleagues have confirmed that the loading processes of  
597 the overlying landslide mass resulted in the substrate liquefaction is key to the  
598 mobility on a flat area (Crosta *et al.*, 2009a; Crosta *et al.*, 2009b; Crosta *et al.*, 2015;  
599 Crosta *et al.*, 2016). The very recent 2014 Oso landslide gained a lot of attentions  
600 about its long runout mobility mechanism. The Oso landslide failed on steep slopes,  
601 and then move along a nearly flat terrace (Iverson *et al.*, 2015; Iverson and George,  
602 2016; Wartman *et al.*, 2016; Stark *et al.*, 2017; Collins and Reid, 2020). However,  
603 these authors argue about the sequential stages of the Oso landslide and what  
604 material was liquefied to explain its long runout mobility on the nearly flat alluvial  
605 plain.

606 The aforementioned typical examples improve our understanding of the

607 transformed landslide from slides on steep upper slopes to flow along gently terrace  
608 and provide important insight of the base liquefaction of terrace deposits controlling  
609 rapid and long-runout mobility, although disagreement remains regarding  
610 mechanisms involved. However, these example landslides confirm that the unusual  
611 structural and hydrologic configurations on the slope toe and fronted terrace zones  
612 are critical for producing a rapid, long-runout landslide overriding terrace deposits.

613

#### 614 **4.2 Rapid and long-runout mobility overridden on a liquefied substrate**

615 There should be similar transformed and mobilized mechanisms between  
616 Saleshan landslide and these landslides mentioned above. The landslides detected  
617 on steep upper slopes transformed into flow-type landslides, causing a rapid and  
618 long-runout mobility overridden on the sand substrate on the nearly flat or gentle  
619 terrace with enough water. Overall, there can divide into two stages after slope  
620 failure. One is the instantaneous transformation of movement style at the toe of the  
621 slope; the second is then long-runout mobility on the fronted terrace. They are both  
622 attributed to dynamic loading from upper landslide mass on the lower liquefied  
623 substrate, which is generally composed of alluvial sand and silt of terrace deposits.  
624 And consequentially, the impact loading results in the generation of excess pore  
625 water pressure on the liquefied sand at the toe of the terrace deposits under  
626 undrained condition, causing a dramatic decrease in shear resistance of the  
627 saturated sand. Nevertheless, there has an essential difference during transformation  
628 and mobility. The transformed moment should be in an undrained condition with

629 almost constant pore water pressure, along with a lower shear resistance. While the  
630 mobilized progress is more like a drained condition with almost constant shear  
631 resistance, comparing continuously dissipated pore water pressure. Our triaxial  
632 dynamic impact loading provides a reasonable explanation for the hypothesized  
633 mechanism to transformation and mobility (Figs. 12). This mechanism is consistent  
634 with those obtained in physical and numerical simulations performed by other  
635 authors (Take and Beddoe, 2014; Crosta et al., 2016; Collins and Reid, 2020).

636       It is worth to mention another type of the transformed landslide from slide to  
  
637 flow coupled with a channel bed erosion along its flow paths. In these events, the  
638 displaced materials after failure entrain and liquefy saturated soil from its flow paths  
639 along the channel on a slope (Evans *et al.*, 2001; Wang *et al.*, 2003; Hungr and Evans,  
640 2004; Iverson *et al.*, 2011). There also had a typical case study in Chinese loess areas,  
641 i.e., the Dagou loess flowslide with significant entrainment (Peng *et al.*, 2015; Zhang  
642 *et al.*, 2017). The underlying process of entrainment and liquefaction is a rapid  
643 undrained loading from the overriding landslide mass. As the dynamic undrained  
644 loading leads to an increase in pore water pressure (Hutchinson and Bhandari, 1971;  
645 Sassa and Wang, 2005; Wang *et al.*, 2013), and liquefy the underlying deposits on the  
646 channel (Wang *et al.*, 2013; Collins and Reid, 2020), causing entrainment of landslide  
647 with higher volume and greater mobility (Hungr and Evans, 2004). As the  
648 channelizing topography can focus landslide momentum (Iverson *et al.*, 2015), and  
649 wet bed deposit can enhance its mobilized capacity (Iverson *et al.*, 2011; Iverson *et*

650 *al.*, 2015). In the study to the 2014 Oso landslide, however, Iverson *et al.* (2015)  
651 pointed out that the transformed landslide into a nearly flat surface is unlike virtually  
652 all the flow along the channelling path. This is because, as suggested by Hutchinson  
653 and Bhandari (1971), the rapid mobility overridden on a nearly flat slope partakes  
654 more of mass transport than the mass movement.

655 Hence, the transformation from slide to flow includes two modes due to  
656 topographic differences. However, there is the same increase in pore water pressure  
657 in the liquefied substrate triggered by dynamic loading (Fig. 14). Meanwhile, the  
658 transformation of the two movement types is both transients to the generation of  
659 pore water pressure in the erosional layer, and the followed long-runout mobility  
660 depends on topographic change and dissipated time of the pore water pressure.

661

## 662 **5. Conclusions**

663 The flowslide overridden on a liquified substrate generally mobilized on a nearly  
664 flat flow path, causing rapid long-runout distance and catastrophic threats. We  
665 studied the Saleshan landslide of Gansu in China, which is a typical loess flowslide  
666 mobilized on the nearly flat terrace with an easily liquefied alluvial sand substrate.  
667 The geomorphologic imprints and topographic changes present the different  
668 dynamic features and mobilized behaviors at different zones of the Saleshan  
669 landslide. And its accumulated features and the placemarks show that the landslide  
670 exists a motion transformation from the slide on the steep slope to flow on the  
671 gentle terrace with rapid velocity and long-runout distance. Meanwhile, ERT

672 surveying confirms the existence of abundant groundwater in the accumulation zone  
673 of the Saleshan landslide, which is crucial to the motion transformation.

674 Our triaxial shear tests suggest that loess, alluvial sand, and red soil are sensitive  
675 to liquefaction at the undrained conditions. Among them, the loess is the easiest  
676 liquefaction. The impact loading test results show that the alluvial sand is natural  
677 liquefaction at undrained condition while it is difficult to drained condition due to  
678 rapid water pore pressure dissipation. This aggravated the occurrence of the  
679 mobilized loess. As a result, the progress enhanced the mobilization of the Saleshan  
680 landslide on the nearly flat terrace. Overall, we conclude that the hydrologic  
681 condition of the terrace is essential to the movement of the Saleshan landslide, and  
682 the liquefaction features of the materials are the key to its transformation during the  
683 landslide's movement. Meanwhile, this kind of flowslide overridden on the liquified  
684 substrate partakes more of mass transport than a mass movement.

685

## 686 **Acknowledgments**

687 This study was partially supported by the National Natural Science Foundation of  
688 China (Nos. 41977212, 41790443 and 41927806), the National Key Research and  
689 Development Program of China (No. 2018YFC504702). Mr. Xishan Lin, Mr. Shuaijun  
690 Hu, and Mr. Xiaoming Feng of Lanzhou University are thanked for their help in the  
691 field investigation. Yao Jiang acknowledges support from the CAS Pioneer Hundred  
692 Talents Program. Images of the geographic, topographic, geomorphic maps and  
693 photographs used for this paper are properly cited and referenced. Original data

694 from ERT, particle size distribution and triaxial shear test are available upon request  
695 (zhangfy@lzu.edu.cn).

696

## 697 **References**

- 698 Aaron, J., Hungr, O., Stark, T.D., Baghdady, A.K., 2017. Oso, Washington, landslide of March 22, 2014:  
699 Dynamic analysis. *Journal of Geotechnical & Geoenvironmental Engineering* 143.
- 700 Bogiatzis, P., 2015. Revitalizing decades-old analog seismograms through image analysis and  
701 digitization. *Mathwork, Technical Articles and Newsletters*,  
702 [https://www.mathworks.com/company/newsletters/articles/revitalizing-decades-old-analog-](https://www.mathworks.com/company/newsletters/articles/revitalizing-decades-old-analog-seismograms-through-image-analysis-and-digitization.html?s_tid=srchtitle)  
703 [seismograms-through-image-analysis-and-digitization.html?s\\_tid=srchtitle](https://www.mathworks.com/company/newsletters/articles/revitalizing-decades-old-analog-seismograms-through-image-analysis-and-digitization.html?s_tid=srchtitle).
- 704 Burda, J., Veselý, M., Řehoř, M., Vilímeck, V., 2018. Reconstruction of a large runout landslide in the  
705 Krušné hory Mts. (Czech Republic). *Landslides* 15, 423-437.
- 706 Carraro, J.A.H., Prezzi, M., Salgado, R., 2009. Shear strength and stiffness of sands containing plastic or  
707 nonplastic fines. *Journal of Geotechnical and Geoenvironmental Engineering* 135, 1167-1178.
- 708 Chambers, J., Meldrum, P., Gunn, D., Wilkinson, P., Merritt, A., Murphy, W., West, J., Kuras, O., Haslam,  
709 E., Hobbs, P., 2013. Geophysical-geotechnical sensor networks for landslide monitoring. *Landslide*  
710 *Science and Practice*. Springer, pp. 289-294.
- 711 Collins, B.D., Reid, M.E., 2020. Enhanced landslide mobility by basal liquefaction: The 2014 State Route  
712 530 (Oso), Washington, landslide. *GSA Bulletin* 132, 451-476.
- 713 Crawford, M.M., Bryson, L.S., Woolery, E.W., Wang, Z., 2019. Long-term landslide monitoring using  
714 soil-water relationships and electrical data to estimate suction stress. *Engineering Geology* 251, 146-  
715 157.
- 716 Crosta, G., Imposimato, S., Roddeman, D., 2009a. Numerical modeling of 2-D granular step collapse  
717 on erodible and nonerodible surface. *Journal of Geophysical Research: Earth Surface* 114.
- 718 Crosta, G.B., Blasio, F.V., Caro, M., Volpi, G., Imposimato, S., Roddeman, D., 2016. Modes of  
719 propagation and deposition of granular flows onto an erodible substrate: experimental, analytical, and  
720 numerical study. *Landslides*, 1-22.
- 721 Crosta, G.B., Blasio, F.V.D., Locatelli, M., Imposimato, S., Roddeman, D., 2015. Landslides falling onto a  
722 shallow erodible substrate or water layer: an experimental and numerical approach. *IOP Conference*  
723 *Series: Earth and Environmental Science* 26, 012004.
- 724 Crosta, G.B., Imposimato, S., Roddeman, D., 2009b. Numerical modelling of entrainment/deposition in  
725 rock and debris-avalanches. *Engineering Geology* 109, 135-145.
- 726 Derbyshire, E., Meng, X.M., Dijkstra, T.A., 2000. *Landslides in the Thick Loess Terrain of North-West*  
727 *China*. Wiley.
- 728 Dufresne, A., Geertsema, M., 2020. Rock slide-debris avalanches: flow transformation and hummock  
729 formation, examples from British Columbia. *Landslides*, 1-18.
- 730 Evans, S.G., Hungr, O., Clague, J.J., 2001. Dynamics of the 1984 rock avalanche and associated distal  
731 debris flow on Mount Cayley, British Columbia, Canada; implications for landslide hazard assessment  
732 on dissected volcanoes. *Engineering Geology* 61, 29-51.
- 733 Grandjean, G., Gourry, J.C., Sanchez, O., Bitri, A., Garambois, S., 2011. Structural study of the Ballandaz

734 landslide (French Alps) using geophysical imagery. *Journal of Applied Geophysics* 75, 531-542.

735 Huang, R., 2009. Some catastrophic landslides since the twentieth century in the southwest of China.

736 *Landslides* 6, 69-81.

737 Hungr, O., Evans, S.G., 2004. Entrainment of debris in rock avalanches: An analysis of a long run-out

738 mechanism. *Geological Society of America Bulletin* 116, 1240-1252.

739 Hungr, O., Leroueil, S., Picarelli, L., 2014. The Varnes classification of landslide types, an update.

740 *Landslides* 11, 167-194.

741 Hutchinson, J.N., Bhandari, R.K., 1971. Undrained loading, a fundamental mechanism of mudflows and

742 other mass movements. *Géotechnique* 21, 353-358.

743 Ishihara, K., Okusa, S., Oyagi, N., Ischuk, A., 1990. Liquefaction-induced flowslide in the collapsible

744 loess deposit in Soviet Tajik. *Soils and Foundations* 30, 73-89.

745 Iverson, R.M., George, D.L., 2016. Modelling landslide liquefaction, mobility bifurcation and the

746 dynamics of the 2014 Oso disaster. *Géotechnique* 66, 175-187.

747 Iverson, R.M., George, D.L., Allstadt, K., Reid, M.E., Collins, B.D., Vallance, J.W., Schilling, S.P., Godt,

748 J.W., Cannon, C.M., Magirl, C.S., Baum, R.L., Coe, J.A., Schulz, W.H., Bower, J.B., 2015. Landslide

749 mobility and hazards: implications of the 2014 Oso disaster. *Earth and Planetary Science Letters* 412,

750 197-208.

751 Iverson, R.M., Reid, M.E., LaHusen, R.G., 1997. Debris-flow mobilization from landslides. *Annual*

752 *Review of Earth and Planetary Sciences* 25, 85-138.

753 Iverson, R.M., Reid, M.E., Logan, M., LaHusen, R.G., Godt, J.W., Griswold, J.P., 2011. Positive feedback

754 and momentum growth during debris-flow entrainment of wet bed sediment. *Nature Geoscience* 4,

755 116-121.

756 Kang, C., Zhang, F., Pan, F., Peng, J., Wu, W., 2018. Characteristics and dynamic runout analyses of

757 1983 Saleshan landslide. *Engineering Geology* 234, 181-195.

758 Kramer, S.L., 1988. Triggering of liquefaction flow slides in coastal soil deposits. *Engineering Geology*

759 26, 17-31.

760 Li, P., Shen, W., Hou, X., Li, T., 2019. Numerical simulation of the propagation process of a rapid flow-

761 like landslide considering bed entrainment: A case study. *Engineering Geology* 263, 105287.

762 Ma, J., Qian, J., 1998. Prediction and evaluation of the influence on environmental hydrogeology in

763 nalesi irrigation district of Baxiehe River Basin. *Journal of Lanzhou University* 34, 106-111.

764 Mangeney, A., 2011. Landslide boost from entrainment. *Nature Geoscience* 4, 77-78.

765 Miao, T., Liu, Z., Niu, Y., Ma, C., 2001. A sliding block model for the runout prediction of high-speed

766 landslides. *Canadian Geotechnical Journal* 38, 217-226.

767 Misfeldt, G.A., Sauer, E.K., Christiansen, E.A., 1991. The Hepburn landslide: an interactive slope-

768 stability and seepage analysis. *Canadian Geotechnical Journal* 28, 556-573.

769 Paguican, E.M.R., Wyk de Vries, B., Lagmay, A.M.F., 2014. Hummocks: how they form and how they

770 evolve in rockslide-debris avalanches. *Landslides* 11, 67-80.

771 Pavoni, N., 1968. Über die Entstehung der Kiesmassen im Bergsturzgebiet von Bonaduz-Reichenau

772 (Graubünden). *Eclogae Geol. Helv* 61/2, 494-500.

773 Peng, D., Xu, Q., Zhang, X., Xing, H., Zhang, S., Kang, K., Qi, X., Ju, Y., Zhao, K., 2019. Hydrological

774 response of loess slopes with reference to widespread landslide events in the Heifangtai terrace, NW

775 China. *Journal of Asian Earth Sciences* 171, 259-276.

776 Peng, J., Fan, Z., Wu, D., Zhuang, J., Dai, F., Chen, W., Zhao, C., 2015. Heavy rainfall triggered loess-

777 mudstone landslide and subsequent debris flow in Tianshui, China. *Engineering Geology* 186, 79-90.

778 Peng, J., Ma, P., Wang, Q., Zhu, X., Zhang, F., Tong, X., Huang, W., 2018. Interaction between  
779 landsliding materials and the underlying erodible bed in a loess flowslide. *Engineering Geology* 234,  
780 38-49.

781 Peng, J., Wang, G., Wang, Q., Zhang, F., 2017a. Shear wave velocity imaging of landslide debris  
782 deposited on an erodible bed and possible movement mechanism for a loess landslide in Jingyang,  
783 Xi'an, China. *Landslides* 14, 1503-1512.

784 Peng, J., Zhang, F., Wang, G., 2017b. Rapid loess flow slides in Heifangtai terrace, Gansu, China.  
785 *Quarterly Journal of Engineering Geology and Hydrogeology* 50, 106-110.

786 Perrone, A., Lapenna, V., Piscitelli, S., 2014. Electrical resistivity tomography technique for landslide  
787 investigation: A review. *Earth-Science Reviews* 135, 65-82.

788 Picarelli, L., 2010. Discussion on "A rapid loess flowslide triggered by irrigation in China". *Landslides* 7,  
789 203-205.

790 Poschinger, A.v., Kippel, T., 2009. Alluvial deposits liquefied by the Flims rock slide. *Geomorphology*  
791 103, 50-56.

792 Sassa, K., Wang, G., 2005. Mechanism of landslide-triggered debris flows: Liquefaction phenomena  
793 due to the undrained loading of torrent deposits. *Debris-flow hazards and related phenomena*.  
794 Springer, pp. 81-104.

795 Stark, T.D., Baghdady, A.K., Hungr, O., Aaron, J., 2017. Case Study: Oso, Washington, Landslide of  
796 March 22, 2014—Material Properties and Failure Mechanism. *Journal of Geotechnical and*  
797 *Geoenvironmental Engineering*, 05017001.

798 Sun, D., Bloemendal, J., Rea, D.K., Vandenberghe, J., Jiang, F., An, Z., Su, R., 2002. Grain-size  
799 distribution function of polymodal sediments in hydraulic and aeolian environments, and numerical  
800 partitioning of the sedimentary components. *Sedimentary Geology* 152, 263-277.

801 Taira, A., Scholle, P.A., 1979. Origin of bimodal sands in some modern environments. *Journal of*  
802 *Sedimentary Research* 49, 777-786.

803 Take, W.A., Beddoe, R.A., 2014. Base liquefaction: a mechanism for shear-induced failure of loose  
804 granular slopes. *Canadian Geotechnical Journal*, 496-507.

805 Wang, G., Huang, R., Chigira, M., Wu, X., Lourenço, S.D.N., 2013. Landslide amplification by  
806 liquefaction of runout-path material after the 2008 Wenchuan (M 8.0) Earthquake, China. *Earth*  
807 *Surface Processes and Landforms* 38, 265-274.

808 Wang, G., Sassa, K., Fukuoka, H., 2003. Downslope volume enlargement of a debris slide-debris flow in  
809 the 1999 Hiroshima, Japan, rainstorm. *Engineering Geology* 69, 309-330.

810 Wang, G., Sassa, K., Fukuoka, H., Tada, T., 2007. Experimental study on the shearing behavior of  
811 saturated silty soils based on ring-shear tests. *Journal of Geotechnical and Geoenvironmental*  
812 *Engineering* 133, 319-333.

813 Wang, G., Zhang, D., Furuya, G., Yang, J., 2014. Pore-pressure generation and fluidization in a loess  
814 landslide triggered by the 1920 Haiyuan earthquake, China: A case study. *Engineering Geology* 174,  
815 36-45.

816 Wang, S., Zhang, Z., Zhan, Z., Liu, H., 1988. On the characteristics and dynamics of the catastrophic  
817 Mount Sale landslide, Gansu. *Journal Chengdu College of Geology* 15, 58-63.

818 Wartman, J., Montgomery, D.R., Anderson, S.A., Keaton, J.R., Benoît, J., dela Chapelle, J., Gilbert, R.,  
819 2016. The 22 March 2014 Oso landslide, Washington, USA. *Geomorphology* 253, 275-288.

820 Wheaton, J.M., Brasington, J., Darby, S.E., Sear, D.A., 2010. Accounting for uncertainty in DEMs from  
821 repeat topographic surveys: improved sediment budgets. *Earth Surface Processes and Landforms* 35,

822 136-156.

823 Wheaton, J.M., Fryirs, K.A., Brierley, G., Bangen, S.G., Bouwes, N., O'Brien, G., 2015. Geomorphic  
824 mapping and taxonomy of fluvial landforms. *Geomorphology* 248, 273-295.

825 Wilkinson, P., Chambers, J., Uhlemann, S., Meldrum, P., Smith, A., Dixon, N., Loke, M.H., 2016.  
826 Reconstruction of landslide movements by inversion of 4-D electrical resistivity tomography  
827 monitoring data. *Geophysical Research Letters* 43, 1166-1174.

828 Wu, W., Wang, N., 2006. *Landslide hazards in Gansu*. Lanzhou University Press, Gansu, China.

829 Xu, L., Dai, F., Kwong, A., Tham, L., Tu, X., 2009. Analysis of some special engineering-geological  
830 problems of loess landslide. *Chinese Journal of Geotechnical Engineering* 31, 287-293.

831 Zhang, F., Kang, C., Chan, D., Zhang, X., Pei, X., Peng, J., 2017. A study of a flowslide with significant  
832 entrainment in loess areas in China. *Earth Surface Processes and Landforms* 42, 2295-2305.

833 Zhang, F., Wang, G., 2018. Effect of irrigation-induced densification on the post-failure behavior of  
834 loess flowslides occurring on the Heifangtai area, Gansu, China. *Engineering Geology* 236, 111-118.

835 Zhang, F., Wang, G., Kamai, T., Chen, W., 2014. Effect of pore water chemistry on undrained shear  
836 behaviour of saturated loess. *Quarterly Journal of Engineering Geology and Hydrogeology* 47, 201-  
837 210.

838 Zhang, F., Wang, G., Kamai, T., Chen, W., Zhang, D., Yang, J., 2013. Undrained shear behavior of  
839 saturated loess with different concentrations of sodium chlorate solution. *Engineering Geology* 155,  
840 69-79.

841 Zhang, F., Yan, B., Feng, X., Lan, H., Kang, C., Lin, X., Zhu, X., Ma, W., 2019. A rapid loess mudflow  
842 triggered by the check dam failure in a bulldoze mountain area, Lanzhou, China. *Landslides* 16, 1981-  
843 1992.

844 Zhang, Z., Chen, S., Tao, L., 2002. 1983 Sale Mountain landslide, Gansu Province, China. *Reviews in*  
845 *Engineering Geology* 15, 149-164.

846 Zhang, Z., Wang, S., 1984. On the prediction of the occurrence time and the velocity of a potential  
847 landslide. *Proceedings, 4th International Symposium on Landslides, Toronto, Canada*, pp. 145-146.

848 Zhuang, J., Peng, J., 2014. A coupled slope cutting—a prolonged rainfall-induced loess landslide: a 17  
849 October 2011 case study. *Bulletin of Engineering Geology and the Environment* 73, 997-1011.

850 **Figure captions**

851 Fig. 1 Geographical location and reviews of the Saleshan landslide. (a) Location of the  
852 Saleshan landslide in Gansu Province, China; (b) Landslide inventory of Baxie River  
853 catchment; (c) Panoramic photograph of the Saleshan landslide in 1983 (Courtesy of  
854 Y. Wang); (d) Panoramic photograph of the Saleshan landslide in 2015.

855 Fig. 2 Simplified stratigraphic and topographic section of the Saleshan landslide. (a)  
856 Before slope failure; (b) After slope failure.

857 Fig. 3 Geomorphologic map of Saleshan landslide. 1 Depletion zone; 2 Accumulation  
858 zone 3 Depressions; 4 Hillocks; 5 Grooves; 6 Hummocks; 7 Main scarp; 8 Minor scarp;  
859 9 Crown cracks; 10 Lateral cracks; 11 Transverse cracks; 12 Radial cracks; 13 Flanks;  
860 14 Contour lines; 15 Gullies; 16 Springs; 17 Baxie River; 18 Jieer reservoir. The boxes  
861 indicate photo locations in Fig. 4, respectively.

862 Fig. 4 Photographs illustrating typical geomorphological imprints of Saleshan  
863 landslide in 1983. (a) Sub-vertical main scarp; (b) Head scarp with depression and  
864 hillock; (c) Standing cow in accumulation zone; (d) Life-saving tree at the toe (photo  
865 from Zhang *et al.*, 2002); (e) Lateral cracks on the east-side at left flank; (f)  
866 Transverse cracks on the west-side at right flank; (g) Transverse cracks on the east-  
867 side at left flank; (h) Radial cracks at the toe; (i) Loess liquefaction at right flank on  
868 accumulation zone; (j) landslide deposition and dammed lake in Baxie River; (k)  
869 Buried Jiuer reservoir and transverse cracks; (l) incompletely liquefied loess on the  
870 east-side accumulation zone. See Fig. 3 for photo locations.

871 Fig. 5 Topographic change detection of pre- and post landslide of the Saleshan

872 landslide. (a) The elevation difference map; (b) the areal change distribution; and (c)  
873 the volumetric elevation change distribution. Black lines indicate the profile locations  
874 in Fig. 6, and red lines show the profile locations of the ERT surveying in Fig. 8.

875 Fig. 6 The topographic changes of alternative profiles of the Saleshan landslide, and  
876 the specified locations see Fig. 5.

877 Fig. 7 Motion displacement vector at different placemark locations on the Saleshan  
878 landslide. 1 Depletion zone; 2 West accumulation zone; 3 Central accumulation zone;  
879 4 East accumulation zone; 5 House location before failure; 6 House location after  
880 failure; 7 Ground marks before failure; 8 Ground marks after failure; 9 Tree location  
881 before and after failure; 10 Life-saving tree before and after failure; 11 Placemark  
882 number.

883 Fig. 8 Interpreted Wenner ERT sections of four profiles on the Saleshan landslide.  
884 Note: the dashed lines are derived from the real topographic profile, and the detailed  
885 locations see Fig. 5 and Fig. 6.

886 Fig. 9 The exemplified particle size distribution of the three types of soils on the  
887 Saleshan landslide. (a) Cumulative distribution curves of particle size; (b) Frequent  
888 distribution curves of particle size.

889 Fig. 10 Undrained triaxial test results of the three different specimens at same  
890 confining pressures. (a) Deviator stress versus axial strain; (b) Pore water pressure  
891 versus axial strain; (c) Effective stress path

892 Fig. 11 Undrained triaxial test results of the alluvial sand specimens at different  
893 confining pressures. (a) Deviator stress versus axial strain; (b) Pore water pressure

894 versus axial strain; (c) Effective stress path

895 Fig. 12 Triaxial test results from quasi-dynamic impact stress loading of the alluvial  
896 sand specimens. (a) drained impact loading condition; (b) undrained impact loading  
897 condition.

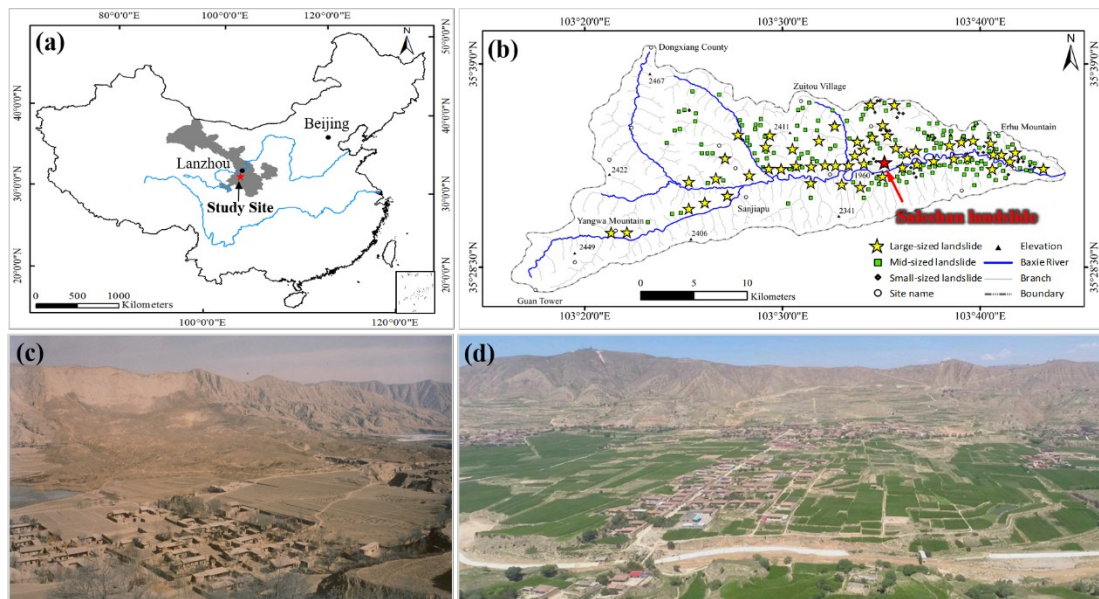
898 Fig. 13 Hypothesised sequence from progressive deformation to the catastrophic  
899 mobility of the Saleshan landslide.

900 Fig. 14 Schematic illustration of two types of entrainment. (a) Mobility overridden on  
901 the liquefied substrate on nearly flat flow path; (b) Mobility eroded the liquefied  
902 layer in relatively steep channel flow path.

903

904  
905  
906

Fig. 1

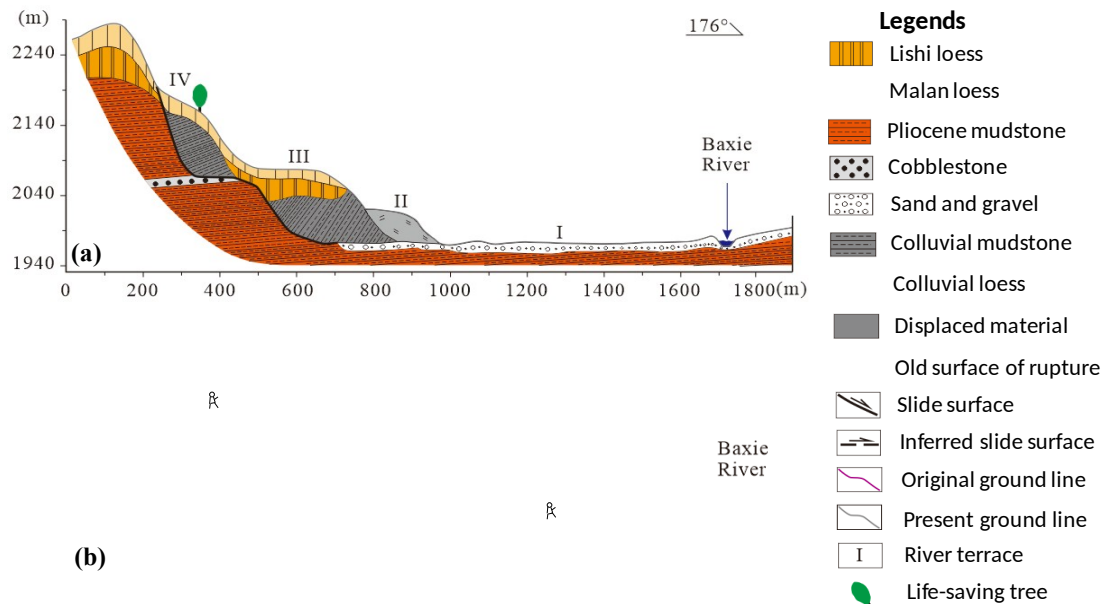


907

908

909 Fig. 2

910

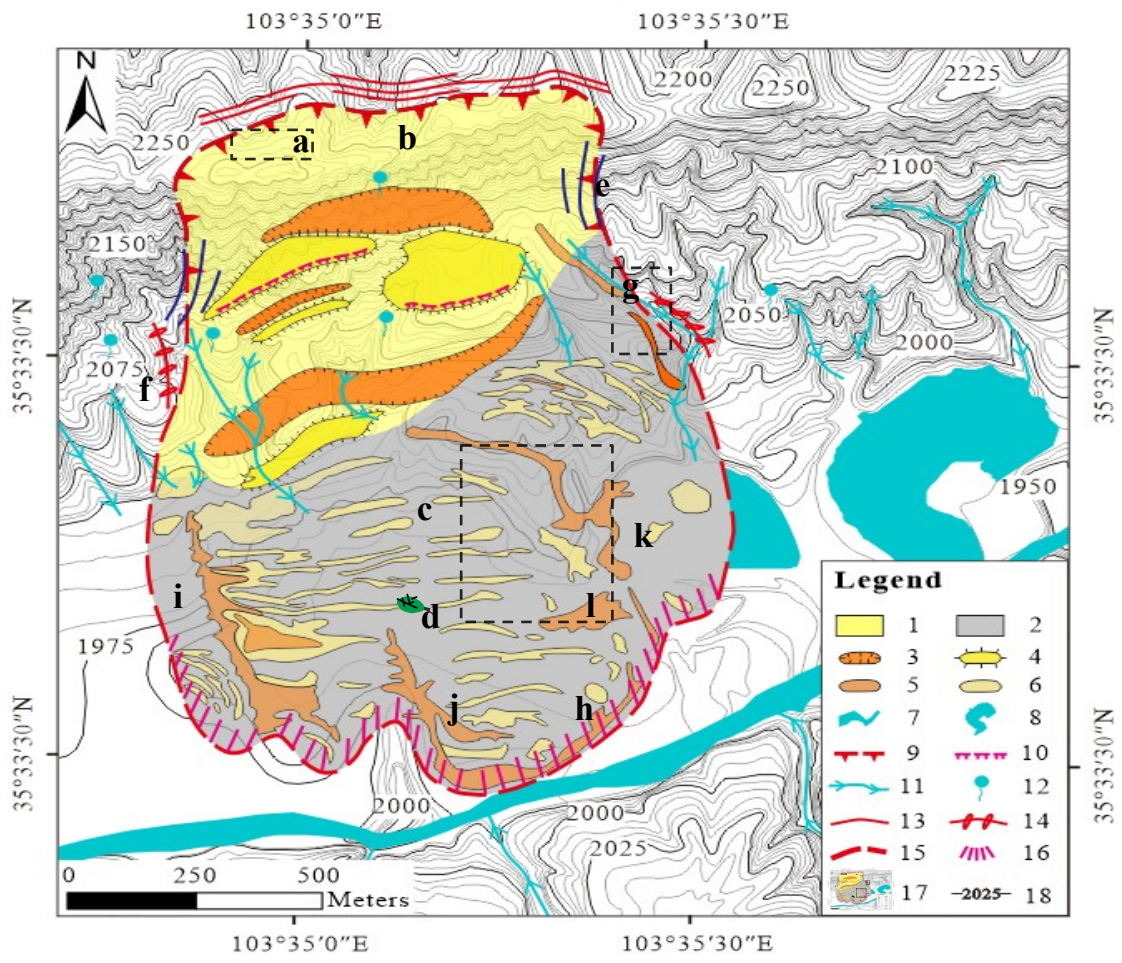


911

912

913  
914  
915

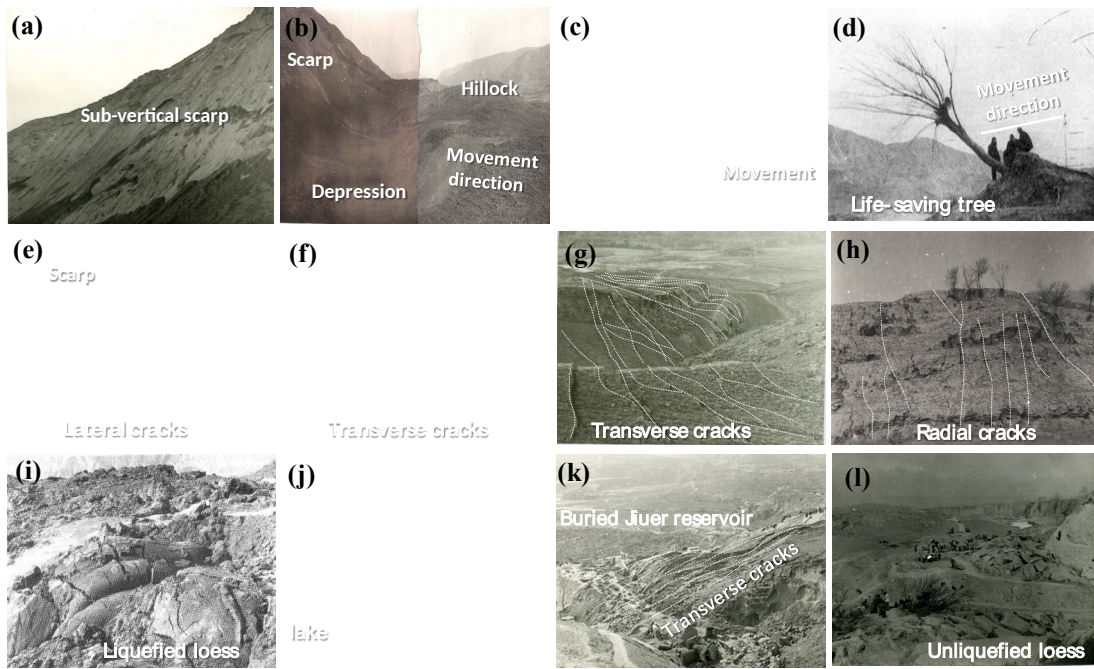
Fig. 3



916  
917

918  
919  
920

Fig. 4

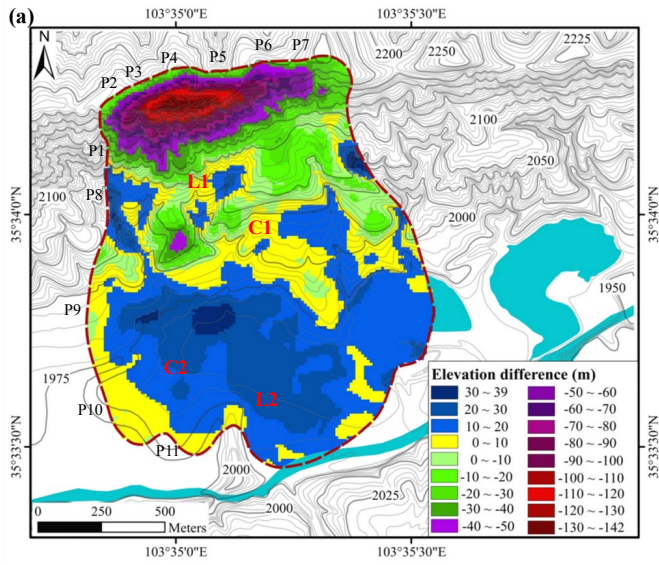


921  
922

923

924 Fig. 5

925

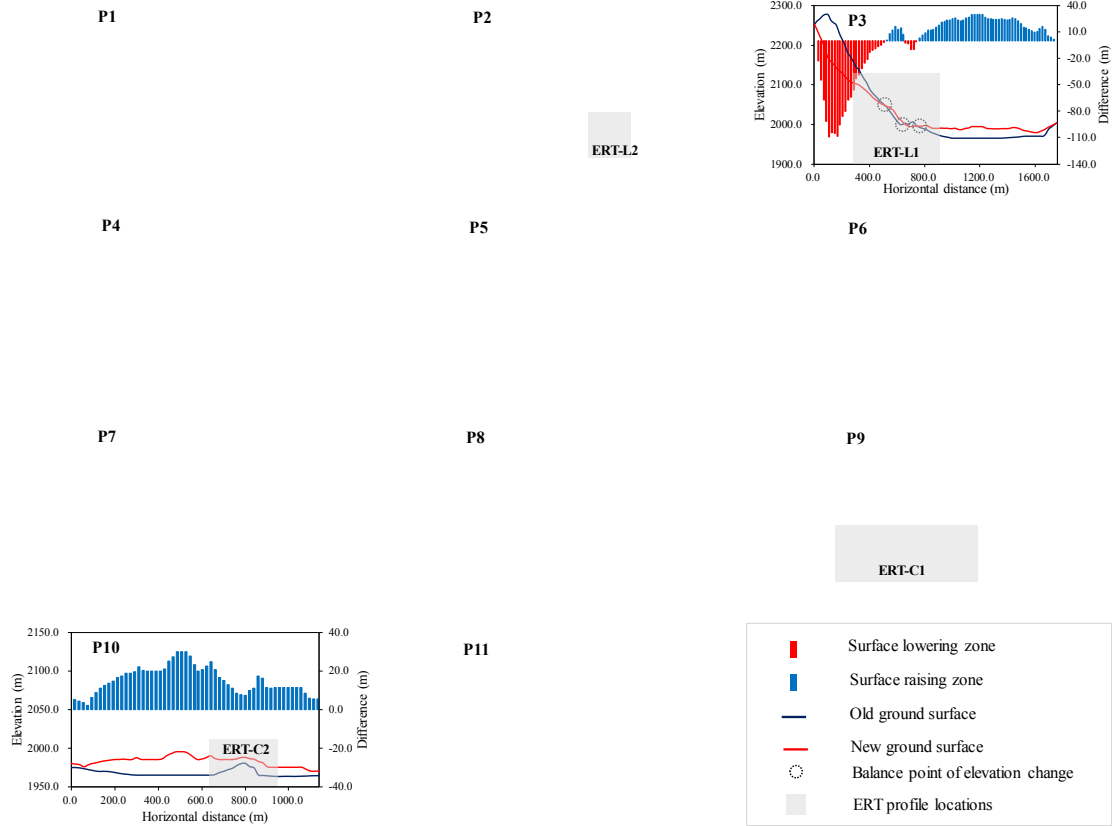


926

927

928  
929  
930

Fig. 6

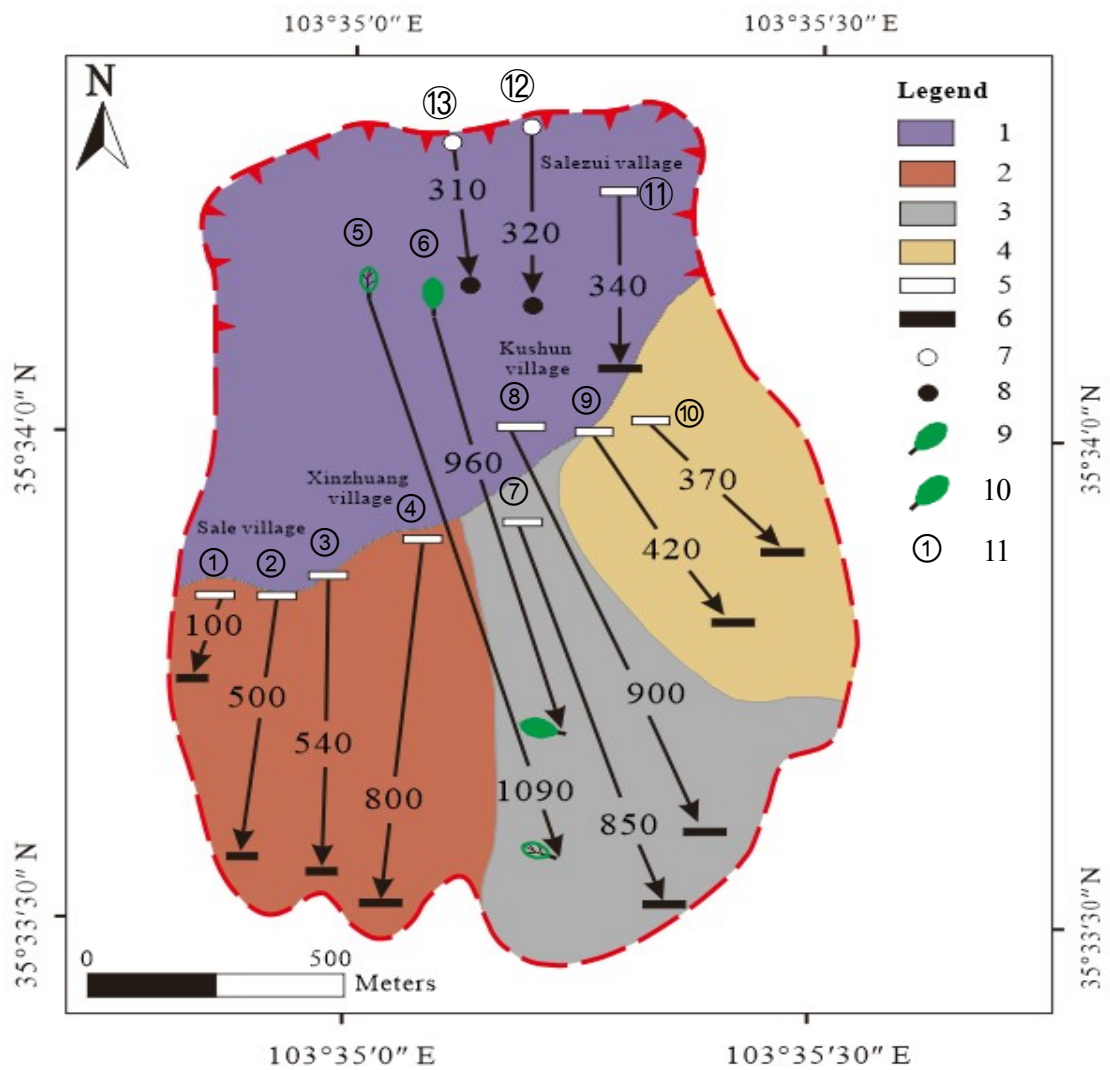


931  
932  
933

934

935 Fig. 7

936

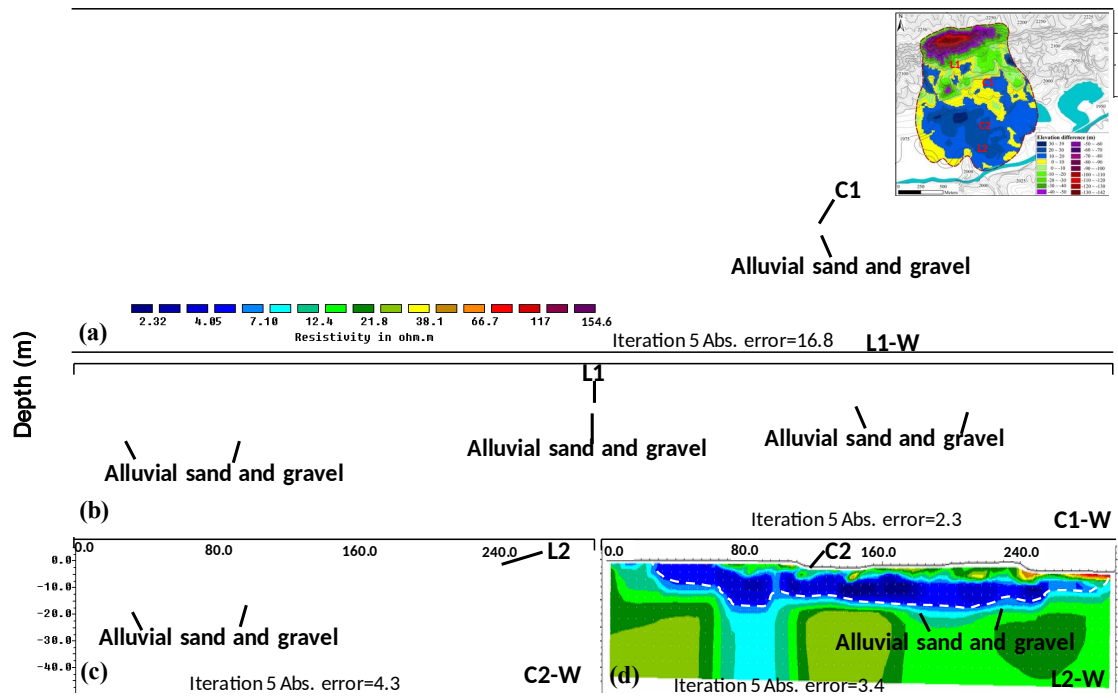


937

938

939  
940  
941

Fig. 8

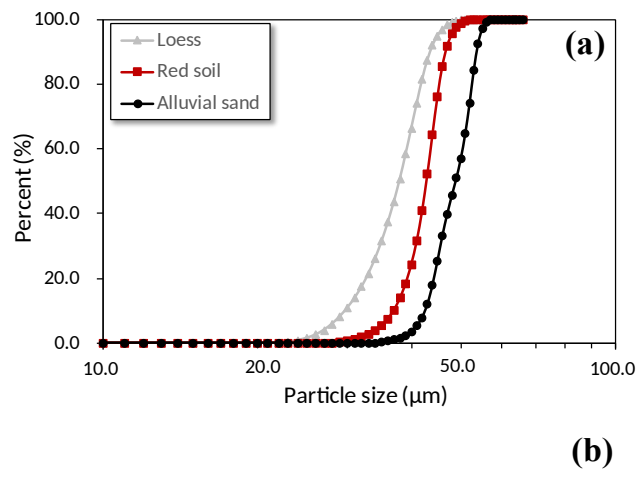


942  
943

944

945 Fig. 9

946



(b)

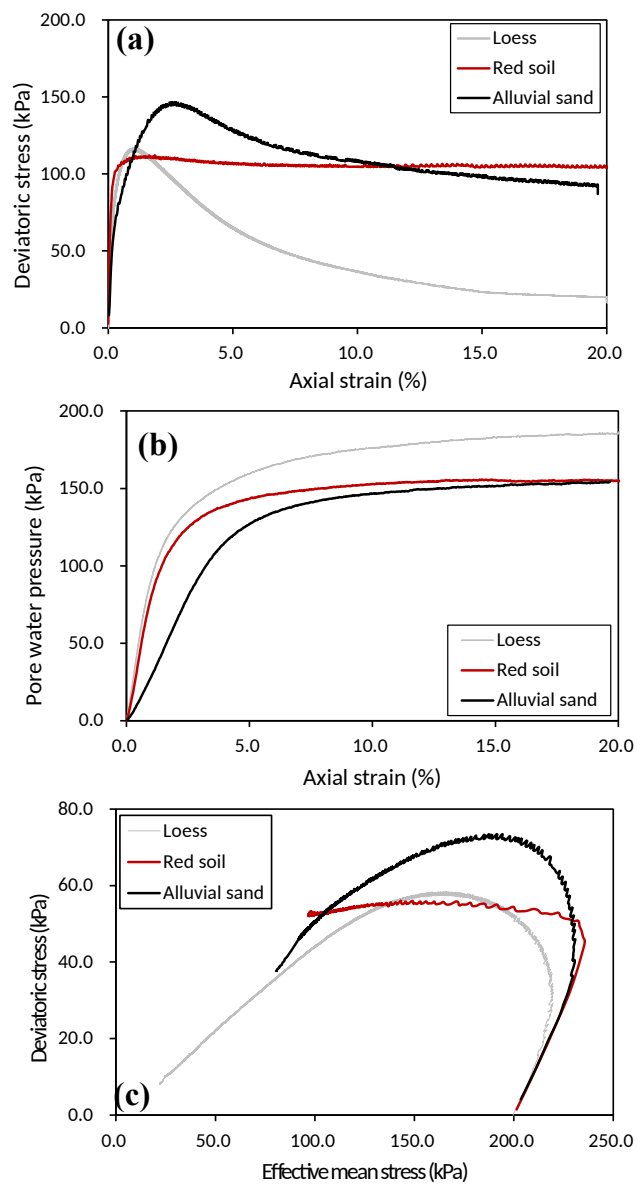
947

948

949

950 Fig. 10

951



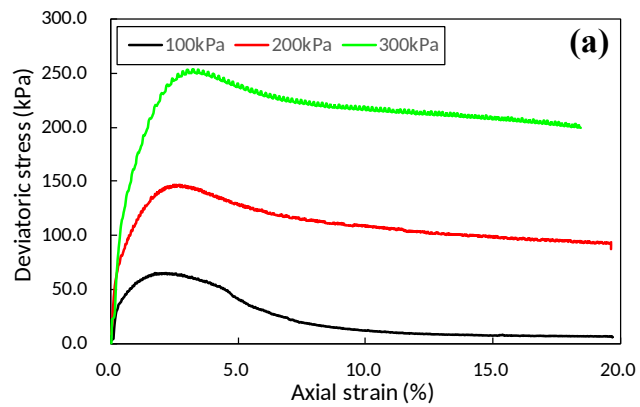
952

953

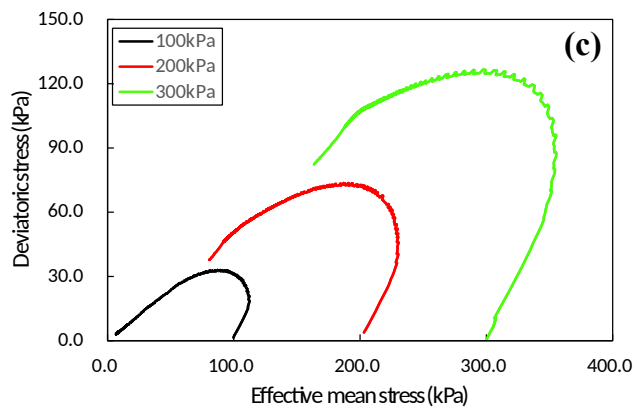
954

955 Fig. 11

956



(b)



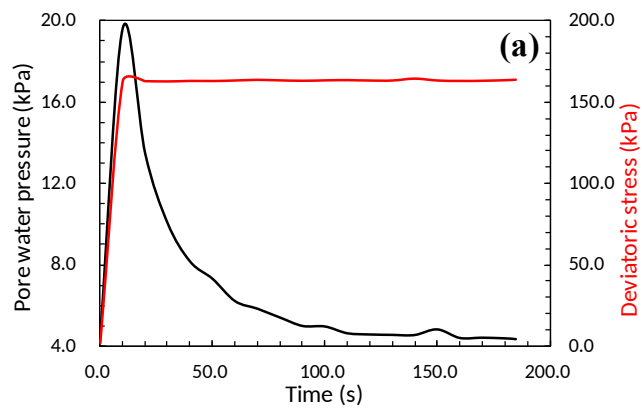
957

958

959

960 Fig. 12

961



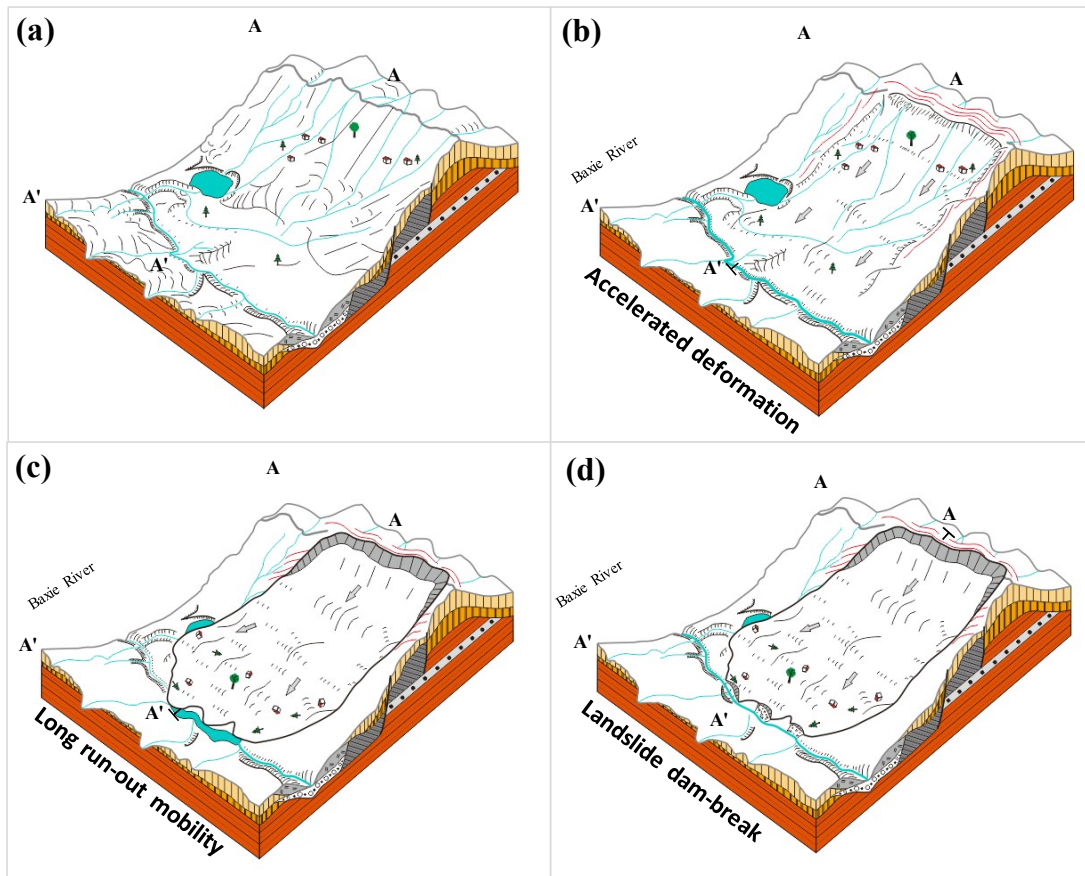
(b)

962

963

964

965 Fig. 13

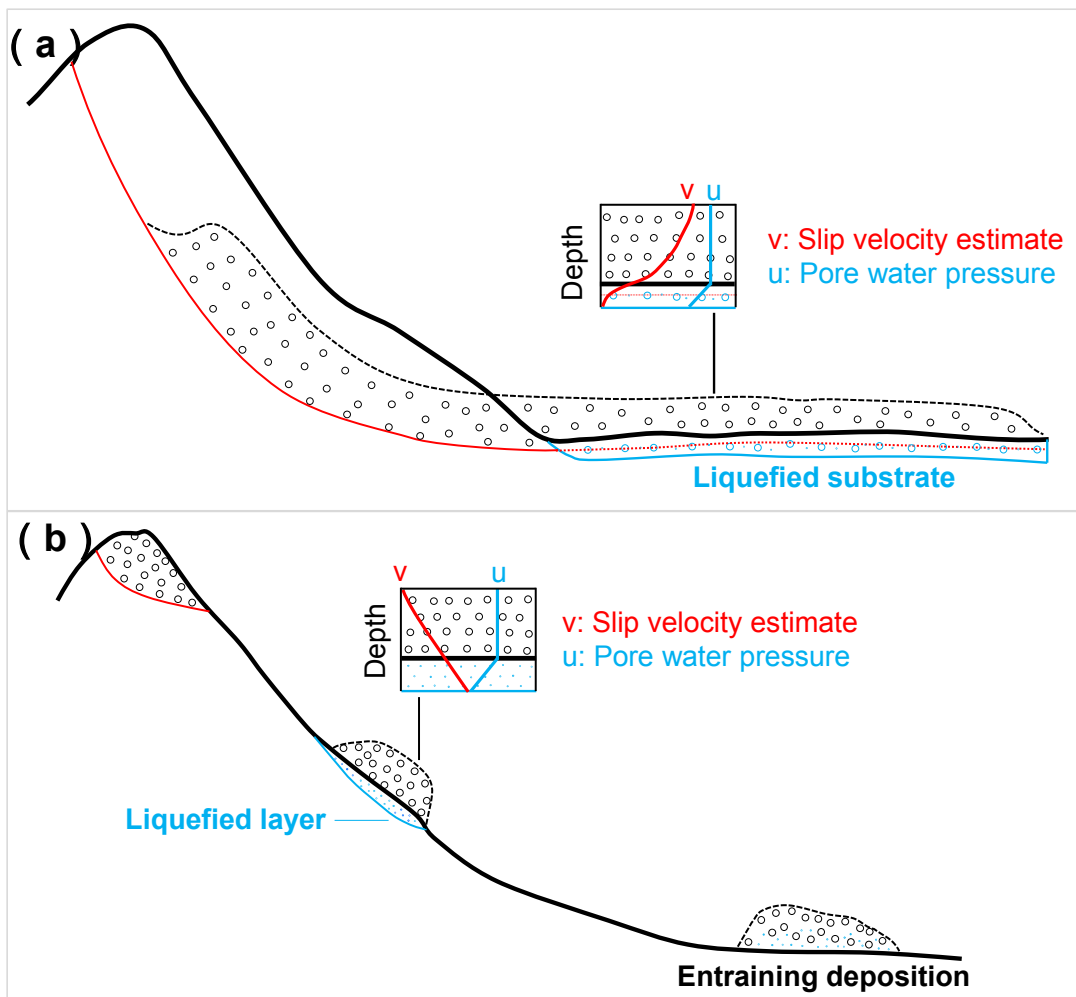


966

967

968 Fig. 14

969



970

971

972 Table 1: Kinematic parameters of different placemark locations on the Saleshan

973 landslide

No.	PL	TD (°)	HD (m)	V (m/s)	AV (m/s)
1		195	100	1.8	
2	WAZ	187	500	9.1	8.8
3		183	540	9.8	
4		188	800	14.5	
5		167	1090	19.8	
6	CAZ	173	960	17.5	16.7
7		170	850	15.5	
8		166	900	16.4	
9	EAZ	150	420	7.6	7.2
10		149	370	6.7	
11		179	340	6.2	
12	DZ	180	320	5.8	5.9
13		175	310	5.6	

974 Note, No.: Placemark number; PL: Placemark location; TD: Travel direction; HD:

975 Horizontal displacement; V: Velocity; AV: Average velocity; WAZ: West accumulation

976 zone; CAZ: Central accumulation zone; EAZ: East accumulation zone; DZ: Depletion

977 zone.